

pubs.acs.org/JPCC Article

Chemical-Composition Tuning-Enabled Optimization of Structure, Properties, and Performance of Lead-Free

(1 - x)BaZr_{0.05}Ti_{0.95}O₃-(x)Ba_{0.92}Ca_{0.08}TiO₃ Electroceramics

Swati K. Gaikwad, Shahaji P. Kharat, Bharat G. Baraskar, Paul G. Nalam, Ajit R. James, Yesh D. Kolekar,* and C. V. Ramana*



Cite This: J. Phys. Chem. C 2024, 128, 2130-2146



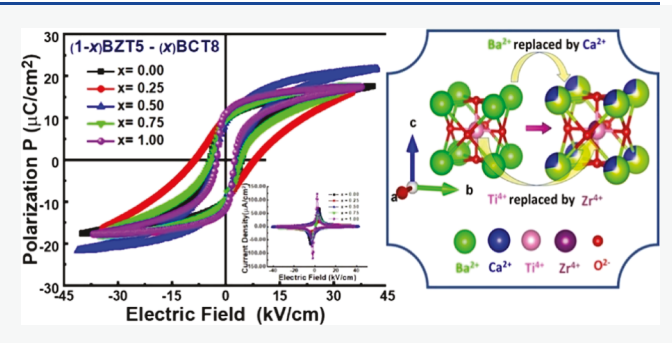
ACCESS I

III Metrics & More

Article Recommendations

Supporting Information

ABSTRACT: Barium titanate (BaTiO₃) and its derivatives, which belong to the family of perovskite oxides, offer a class of lead (Pb)-free ferroelectric and piezoelectric materials with numerous applications in electronic and electromagnetic devices. In this study, we report on the Pb-free materials with a variable composition (1-x)BZT5-(x)BCT8 (x=0.00-1.00) where BZT5 refers to BaZr_{0.05}Ti_{0.95}O₃ and BCT8 refers to Ba_{0.92}Ca_{0.08}TiO₃. The substitution of Zr⁴⁺ for Ti⁴⁺ and Ca²⁺ for Ba²⁺ in the BaTiO₃ matrix enhances the properties and performance desirable for applications involving ferroelectric capacitors and memory storage devices. X-ray diffraction (XRD)



studies coupled with Rietveld refinement analyses confirm the biphasic (major tetragonal and minor orthorhombic) crystal structure of all the samples. Raman spectroscopic studies corroborate with XRD results and validate the biphasic crystal structure. Chemically homogeneous samples exhibit the characteristic granular-dense microstructure. The density measurements using Archimedes' principle indicate that the sample density is above 5.31 g/cm³ (90%). Ferroelectric measurements display typical polarization-electric field (P–E) hysteresis, confirming the ferroelectric nature and electric field-induced strain butterfly (S-E) loops, confirming the piezoelectric nature of all the samples. The dielectric properties of all of the compositions indicate significant prospects for future capacitor applications. Ferroelectric measurements show that BZT5 exhibits a maximum value of 0.70 squareness ratio, indicating that BZT5 can be a suitable material for permanent ferroelectric random-access memory (Fe-RAM) applications, whereas 0.75BZT5–0.25BCT8 is suitable for switching applications. The moderately higher remnant polarization ($P_r = 11.22 \, \mu \text{C/cm}^2$) and the lower coercive field ($E_c = 2.54 \, \text{kV/cm}$) are obtained for BCT8. The piezoelectric coefficient and strain studies show that sample with x = 0.50 exhibits a higher converse piezoelectric coefficient of $430 \pm 1 \, \text{pm/V}$ and 0.179 (% strain). The Q-factor for the BZT5 composition was observed to be $4.13 \times 10^{-4} \, (\text{cm}^2/\mu\text{C})^2$, which is the maximum among the studied compositions, suggesting that BZT5 may be a suitable candidate for energy conversion transducer applications.

1. INTRODUCTION

Currently, strict rules and regulations are imposed on the use of lead(Pb)-based compounds and electronic materials, which are quite routinely employed in various electronic devices, sensors, actuators, etc.¹⁻⁴ These restrictions started with Restrictions of Hazardous Substances (RoHS) rules implemented by the European Union to eradicate the use of toxic compounds from electronic devices and instruments. Before the RoHS regulation, the well-known PbZr_{0.48}Ti_{0.52}O₃, abbreviated as PZT, was a popular material that was used in most of the electronic devices.^{5,6} The PZT has superior piezoelectric properties among all other Pb-based as well as Pb-free piezoelectric materials. However, due to these regulations, the traditional PZT material is currently disqualified for utilization, as it is dangerous for all living organisms including humans.^{7,8} Similarly, the Pb-based compounds can get easily mixed with the drinking water

sources that can affect the biodiversity of plants and animals. ^{9,10} Thus, the design and development of nontoxic, Pb-free materials, which can replace the traditional Pb-based materials, is highly desirable. ^{11–13} On the other hand, scientifically and technologically, it is a challenging task, which urges the scientific and engineering community to direct attention with rigorous research and development activities. ^{14–16}

Received: October 18, 2023
Revised: December 15, 2023
Accepted: December 28, 2023
Published: January 31, 2024





Toward realization of Pb-free ferroelectrics, BaTiO₃ (BT)based compounds can play a vital role. 17,18 However, in comparison to Pb-based materials such as PZT, the lead-free piezoelectric materials (as BaTiO₃) exhibit poor properties, viz., lower piezoelectric coefficient (d_{33} < 200 pC/N), lower Curie temperature, and higher dielectric loss. Recently, there have been a few successful attempts that made the realization of novel Pb-free materials possible for higher piezoelectric response, $d_{33} = 300$ to 600 pC/N. ^{19,20} In one of these attempts, Liu and Ren have prepared a morphotropic phase boundary (MPB) composition BaZr_{0.20}Ti_{0.80}O₃-0.5Ba_{0.70}Ca_{0.30}TiO₃ (abbreviated as BZT-BCT) and reported the piezoelectric coefficient ($d_{33} \sim 620 \text{ pC/N}$), which is the highest among the known lead-free and environmentally friendly materials.21,22 This report fascinated the scientific community to further explore BT-based lead-free materials with reduced environmental concerns.2

Lead-free BT-based perovskite, i.e. BZT-BCT ceramics, possesses notable dielectric properties, viz., reasonably higher dielectric constant and low dielectric loss, in addition to the enhanced ferroelectric and piezoelectric properties, thus making them suitable for various technological applications. In the (1 - x)BZT5-(x)BCT8 compositions, the x = 0.5samples attracted our attention because of their upgraded and better piezoelectric and ferroelectric properties. Also, this composition had both the tetragonal and rhombohedral phases close to the MPB. 24,25 In connection with the applications of lead-free materials, Parhi et al. have reported a comparative study of lead-free BaZr_{0.2}Ti_{0.8}O₃ ceramics with the leadcontaining $PbZr_{0.52}Ti_{0.48}O_3$ ceramic, with the results indicating that BZT is useful for optoelectronic devices and highfrequency applications, including SONAR and hydrophone. Further, the presence of nearby room-temperature phase transition makes BZT a suitable material for biomedical and underwater applications.²⁶ The Ca²⁺ and Zr⁴⁺ substitutions, respectively, for Ba²⁺ and Ti⁴⁺ in BaTiO₃ ceramics, significantly modify the grain size, densities, and microstructure, which are important factors to tailor the dielectric, ferroelectric, and piezoelectric properties.²⁷ Thus, the (Ba,Ca)(Zr,Ti)O₃ ceramics are expected to demonstrate optimal properties, making them feasible lead-free piezoelectric competitors. In this connection, Yoon and Ur have explored advancements in enhancing dielectric properties of a ceramic material comprising BaTiO₃-CaTiO₃. Their investigation involves strategic substitutions of ions, specifically Ca at the Ba-site and Zr at the Ti-site, along with tin (Sn) substitutions. Accordingly, the compositions with the chemical formula (Ba,Ca)(Ti,Zr,Sn)O₃ were synthesized using the conventional ceramic method, and dielectric properties were systematically studied.²⁸ Furthermore, by focusing on the MPB construction, methods for modifying the dielectric characteristics of BaTiO₃ are reported in the literature with typical candidate materials being $(Ba,Ca)(Zr,Ti)O_3$, $(Ba,Ca)(Sn,Ti)O_3$, and (Ba,Ca)-(Hf,Ti)O₃. Additionally, there were efforts made toward the growth and characterization of some of these compositions in the form of thin films to explore their performance in terms of piezoelectric, ferroelectric, and dielectric characteristics.^{29–31} Keswani et al. have made a comprehensive investigation of lead-free ceramics $Ba_{(1-x)}Ca_xTiO_3$ (x = 0.0-0.3) and $BaTi_{(1-y)}Zr_yO_3$ (y = 0.0-0.2), synthesized via the standard solid-state reaction method.³² Employing first-principles density functional calculations, the electronic structure, dynamical charges, and spontaneous polarization of these

compounds were explored.³² Their study demonstrated enhanced ferroelectric and piezoelectric properties compared with the existing literature, with higher values for polarization, percentage strain, piezoelectric coefficients, and electrostrictive coefficient. It is also reported that, for smaller substitutions of Ca and Zr in BaTiO₃, a direct piezoelectric coefficient (d_{33}) was enhanced.³²

Further, it is important to note that, for getting a higher piezoelectric response, it is difficult to rely only on the phase diagram of the synthesized materials. The reason is even though the Hf-, Zr-, or Sn-substituted BaTiO₃ systems³³⁻³⁵ show a similar phase diagram to that of BZT-BCT, the piezoelectric coefficients observed in Hf-, Zr-, and Snsubstituted barium titanate are significantly lower (d_{33} ~ 300-400 pC/N) compared to BZT-BCT ($d_{33} \sim 600$ pC/ N).21 Thus, while there is a great demand for environmentfriendly Pb-free compounds with improved properties for device applications, the search for alternate Pb-free materials continues. 36-42 Specifically, in the field of ferroelectric capacitors, electronic systems, high-energy devices, electromechanical devices, and transducers and actuators, the main emphasis is on the development of alternate materials compatible to the well-known Pb-based materials. In this connection, BaTiO₃-based (Ba,Ca)(Ti,Sn)O₃, (Ba,Ca)(Ti,Zr)-O₃, and (Ba,Ca)(Ti,Hf)O₃ compositions are recommended as Pb-free piezoelectric materials for advanced technological demands. 30,43-45 These compositions are to be advanced to span their possible applications in detecting various stimuli such as human body motion, electronics, optoelectronics, and magnetoelectric energy harvesting and Fe-RAM applications. 21,30,36-39,43-46

The $BaTiO_3$ -based compositions belong to the perovskite structure with the space group (P4mm), where corner ions are divalent (such as Ba^{2+} , Ca^{2+} , etc.), body-centered ions are tetravalent (such as Ti^{4+} , Zr^{4+} , Sn^{4+} , Hf^{4+} , etc.), and O^{2-} anions are at the face center. Figure 1 shows a schematic

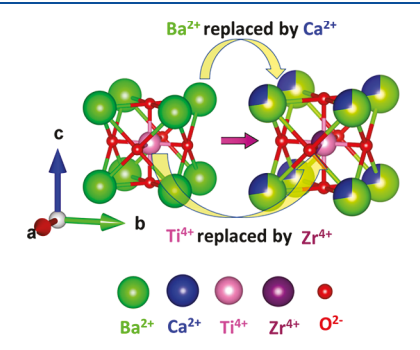


Figure 1. Schematic representation of the tetragonal structure of $BaTiO_3$ and the modified $BaTiO_3$ as Ba^{2+} with Ca^{2+} and Ti^{4+} with Zr^{4+} .

representation of the tetragonal structure and the partial substitution of Ba²⁺ by Ca²⁺ and Ti⁴⁺ by Zr⁴⁺ in the perovskite structure. The noncentrosymmetric Ti⁴⁺ ions are a source of permanent electric dipole moments in BaTiO₃. Despite the fact that the scientific community has been working meticulously to develop Pb-free alternative materials with improved properties, there is no unique material or compound realized so far, especially a contender with all the properties, superior as compared to traditional Pb-based ferroelectrics. Therefore, we have directed our efforts to prepare such

materials with a Pb-free composition, which can fulfill the required properties and performance. He have carefully chosen (1-x)BZT5-(x)BCT8 (x=0.00-1.00; where BZT5 refers to BaZr_{0.05}Ti_{0.95}O₃ and BCT8 refers to Ba_{0.92}Ca_{0.08}TiO₃) materials and deeply investigated their structural, dielectric, ferroelectric, and piezoelectric properties. Specifically, we report on the chemical composition tuning-facilitated optimization of the structural, dielectric, ferroelectric, and piezoelectric properties of (1-x)BZT5-(x)BCT8 materials for practical electronic device applications.

In BZT5 (BaZr_{0.05}Ti_{0.95}O₃), we expect that the Zr⁴⁺ substitution for Ti4+ in BaTiO3 can enhance the chemical stability, increase the Curie temperature, and improve the dielectric constant (i.e., reduce dielectric loss) so that the proposed composition may be suitable for electronic device applications. Additionally, the Zr4+ substitution can also enhance the ferroelectric as well as piezoelectric properties. 50-53 Also, in BCT8 (Ba_{0.92}Ca_{0.08}TiO₃), the substitution of Ca²⁺ for Ba²⁺ in BaTiO₃ is expected to improve the dielectric constant (ε ' = 1655), decreases the dielectric loss (tan δ = 0.013), and increases the curie temperature (T_c) .⁵⁴ Further, the concentration of Ca²⁺ is restricted to 0.08 mol % because of two reasons. First, with Ca²⁺ substitution above 0.25 mol % in the BT sample, a small peak was observed at $2\theta = 32.94^{\circ}$, which corresponds to the CaTiO₃ phase and is responsible for suppressing ferroelectric properties. 55 Second, according to the Landolt-Börnstein series, the x = 0.08 mol % of Ca²⁺ in BT shows a higher Curie temperature and dielectric constant.⁵⁶ Furthermore, we expect that the (1 - x)BZT5-(x)BCT8, with variable compositions, may be one of the possible alternatives to replace toxic Pb-based materials. 3,47,48 Thus, as reported in the paper, we made an attempt to comprehensively study the structural, dielectric, ferroelectric, and piezoelectric properties of the (1 - x)BZT5-(x)BCT8 Pb-free compositions.

2. EXPERIMENTAL DETAILS

2.1. Synthesis. To prepare Pb-free ferroelectric materials with a variable composition, (1 - x)BZT5-(x)BCT8 (x = 0.00, 0.25, 0.50, 0.75, and 1.00), AR grade precursors were used in the standard high-temperature solid-state reaction method. BaCO₃, TiO₂, CaCO₃, and ZrO₂ (all with a purity of 99.9%) were taken in stoichiometric proportion and ball milled using a zirconia ball in ethanol medium for 24 h for uniform mixing. Then, mixed wet powders were heated in an oven at 80 °C and ground for about 1 h with the help of an agate mortar. These powders were then calcined at 1150 °C in air for 10 h with a heating and cooling rate of 2 °C/min. After cooling to room temperature, calcined powders were ground again for homogeneous mixing for 5 h and then presintered at 1260 °C for 10 h. After presintering, the powders were finally ground for 5 h and pressed into cylindrical pellets of diameter ~10 mm and approximate thickness of ~1 mm using a hydraulic press with a 5 ton pressure. For the pellet preparation, 5 wt % polyvinyl alcohol (PVA) was used as a binder. Then, these pellets were finally sintered at 1350 °C for 10 h for densification of pellets and cooled up to 300 °C and then cooled naturally to room temperature. A complete synthesis method is presented in the form of a schematic flowchart in Figure S1 (Supporting Information). The chemical reaction for the synthesis of BZT5, BCT8, and (1 - x)BZT5–(x)BCT8 is shown below

$$BaCO_3 + 0.95TiO_2 + 0.05ZrO_2$$

 $\rightarrow BaZr_{0.05}Ti_{0.95}O_3 + CO_2 \uparrow$ (1)

$$0.92 \text{BaCO}_3 + 0.08 \text{CaCO}_3 + \text{TiO}_2$$

 $\rightarrow \text{Ba}_{0.92} \text{Ca}_{0.08} \text{TiO}_3 + \text{CO}_2 \uparrow$ (2)

$$(1 - x)BaZr_{0.05}Ti_{0.95}O_3 + xBa_{0.92}Ca_{0.08}TiO_3$$

$$\rightarrow (1 - x)BaZr_{0.05}Ti_{0.95}O_3 - xBa_{0.92}Ca_{0.08}TiO_3$$
(3)

2.2. Characterization. 2.2.1. Structural Studies. Structural characterization of the materials was primarily performed by using X-ray diffraction (XRD) and Raman spectroscopic measurements. The XRD measurements were performed using a Bruker D8 Advance X-ray diffractometer (Cu K_{α} having $\lambda =$ 1.5406 Å). The XRD scans were taken with a step size of $0.02^{\circ}/s$ in the 2θ range from 20° to 80° . For structural characterization and chemical bonding analysis, the Raman spectroscopic technique was utilized as it can detect lower percentages of impurity phases and identify crystalline phases with different symmetries, such as the cubic, tetragonal, or orthorhombic phases of BaTiO₃-based compounds.⁵⁷ Raman measurements were performed using a Raman spectrometer (Renishaw In Via microscope Raman with Ar⁺ ion laser, $\lambda =$ 532 nm) in the range of 100–1000 cm⁻¹ at room temperature. In addition, temperature-dependent (-193 to 227 °C) Raman spectroscopic measurements were also performed on all the

2.2.2. Microstructure and Morphology Studies. Surface morphology and microstructure analyses of the samples were carried out using Scanning Electron Microscopy (SEM). During SEM imaging, conducting carbon tape was used for grounding the samples so that the space charges are removed. Energy-Dispersive Spectroscopy (EDS) was used to calculate the atomic and weight percentages of elements present in the samples. The density of the sintered pellets was measured using Archimedes' principle. ⁵⁸

2.2.3. Property Measurements. The (1 - x)BZT5-(x)BCT8 (x = 0.00-1.00) materials were made into pellets, which were then electroded using conductive silver paste, for dielectric, ferroelectric, and piezoelectric properties measurements. The (1 - x)BZT5-(x)BCT8 pellets were polished with sandpaper, and conductive silver paste was applied to the electrical contacts. These silver-pasted pellets were heated at around 100 °C for 1 h. The dielectric measurements were made using a Hioki 3532-50 LCR meter at frequencies ranging from 42 Hz to 1 MHz. To confirm the ferroelectric nature of the samples, polarization versus electric field hysteresis loop measurements (P-E) were performed using a piezoelectric evaluation system, TF analyzer 2000 from M/s aixACCT GmbH. P-E measurements were taken at a frequency of 1 Hz using a triangular waveform. To make electric poling, silverpasted pellets were subjected to an electric field three times the coercive field ($E_{\text{poling}} = 3E_{\text{c}}$) for about half an hour. This poling process is required for polarization switching and prevents dielectric breakdown of pellets due to overpoling. After 24 h of poling, cylindrical pellets were then used to measure direct piezoelectric coefficients (d_{33}) using a Piezo- d_{33} meter with a 250 mN force.

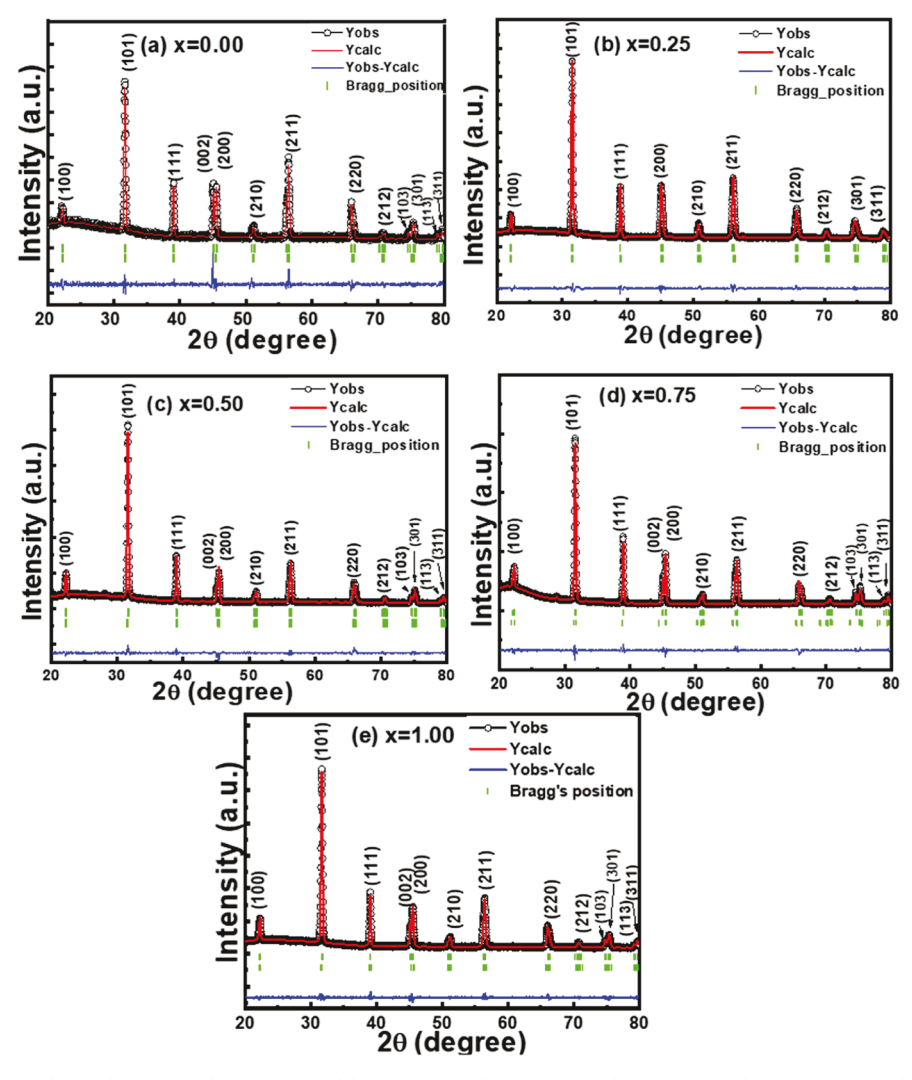


Figure 2. XRD patterns of (1 - x)BZT5 - (x)BCT8 with (a) x = 0.00, (b) x = 0.25, (c) x = 0.50, (d) x = 0.75, and (e) x = 1.00.

Table 1. Rietveld-Refined Structural Parameters and Experimental Density for (1-x)BZT5-(x)BCT8 Compositions

x	phase	a (Å)	b (Å)	c (Å)	c/a ratio	phase (%)	Bragg R factor	$R_{ m f}$ factor	goodness of fit (R_{wp})	χ^2	volume (Å) ³	density (g/cm ³)	density (%)
0.00	T	3.984	3.984	4.023	1.010	74.14	4.53	3.16	1.35	1.83	63.86	5.65	96
	O	3.990	5.659	5.644		25.86	3.15	1.90			127.43		
0.25	T	4.007	4.007	4.027	1.005	64.39	1.61	1.39	1.36	1.83	64.96	5.31	90
	O	4.002	5.690	5.682		35.61	1.98	1.33			129.37		
0.50	T	3.994	3.994	4.025	1.008	67.98	3.89	2.46	1.35	1.82	64.21	5.47	93
	O	3.990	5.668	5.682		32.02	3.58	1.97			128.52		
0.75	T	3.993	3.993	4.028	1.009	95.81	2.45	1.58	1.44	2.09	64.22	5.37	91
	O	4.080	5.645	5.643		4.19	7.5	6.23			129.99		
1.00	T	3.984	3.985	4.017	1.008	94.79	1.79	1.07	1.34	1.78	63.78	5.57	95
	O	3.977	5.653	5.680		5.21	1.76	1.11			127.69		

3. RESULTS AND DISCUSSION

3.1. Crystal Structure and Phase. The XRD data of (1 - x)BZT5-(x)BCT8 compounds are presented in Figure 2. The data shown are the experimental XRD patterns along with the Rietveld refinement calculated patterns. Rietveld refinement fitting is an important method to understand structural properties of the polycrystalline powder samples. ^{59,60} Thus, we have performed refinement on all of the synthesized ferroelectric samples as a function of x. Detailed analyses show that all the samples possess a tetragonal phase (major) and an

orthorhombic phase (minor). No impurity peaks and/or secondary phase was detected in any of the samples. The data confirm the substitution of Zr^{4+} for the Ti^{4+} site in the BZT5 sample and Ca^{2+} for the Ba^{2+} site in BCT8.

The concentration/amount (percentage) of orthorhombic (O) and tetragonal (T) phases observed in all the ferroelectric compositions were calculated using 1

$$phase composition = \left(\frac{A_{phase}}{A_{total}}\right) \times 100\%$$
(4)

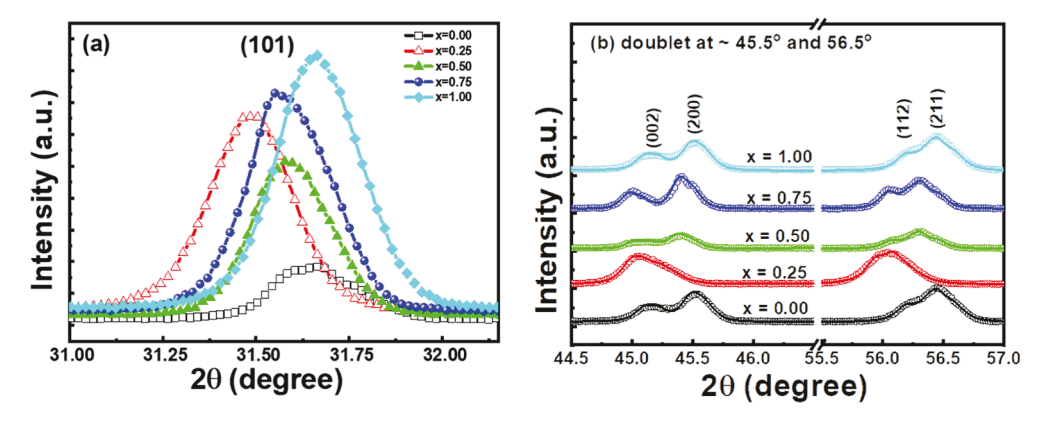


Figure 3. X-ray diffraction patterns. (a) Highest intensity peak (101) of all ferroelectrics. (b) Doublet peaks confirming the tetragonal crystal structure of (1 - x)BZTS - (x)BCT8.

where $A_{\rm phase}$ is the area of the respective phase (T or O) and $A_{\rm total}$ is the cumulative area of all the phases present.

The lattice parameter values and phase percentages determined are listed in Table 1 for all of the samples as a function of x. Figure 3a shows the detailed scan of the highest intensity peak, which corresponds to the (101) reflection, for all the samples. Substitution of a larger size cation causes the lattice constant enhancement. On the other hand, in case of BCT8, the peak shift toward a higher 2θ value can be noted. This may be due to the substitution by a smaller ionic radius cation, i.e., Ca^{2+} (1.34 Å), for larger Ba^{2+} (1.61 Å) in the crystal structure. According to Bragg's diffraction condition, $2d \sin \theta =$ $n\lambda$, if the interatomic distance is decreased, the interplanar spacing (d) also decreases, and thus there will be a shift of the XRD peak toward a higher 2θ angle.⁶³ Figure 3b, which represents the XRD data in a selected narrow region, shows an apparent two doublets at $(2\theta \approx 45.5 \text{ and } 56.5^{\circ})$ for all the samples. In the doublet, the first at $2\theta \approx 45.5^{\circ}$ corresponds to diffraction from the (002) planes, and the second peak corresponds to the diffraction from (200) planes. Similarly, in the second doublet present at $2\theta \approx 56.5^{\circ}$, the two peaks correspond to diffraction from the (112) and (211) planes, respectively.

The presence of these two doublets confirms the tetragonal structure. Further, for x = 0.25 and x = 0.50, the doublet is not clearly seen. This can be attributed to the presence of the orthorhombic phase in a higher quantity, which is about 35.61 and 32.02%, respectively, for x = 0.25 and x = 0.50. Thus, doublet or tetragonality is not clear for the x = 0.25 sample. Also, peak broadening is more for this sample compared to other samples. If tetragonal phase is present, then the c/a ratio for all the samples must be greater than unity. Accordingly, we have observed the results presented in Figure 4, which shows the c/a ratio of the tetragonal phase (T-phase).

3.2. Chemical Bonding. Raman spectroscopy is highly sensitive to the local structure and chemical bonding and provides information about chemical bonds and changes in the crystal structure with the substitution of particular ions in the lattice. Therefore, to understand the chemical bonding and effect of substitution of Ca^{2+} and/or Zr^{4+} ions, we relied on Raman spectroscopic measurements on all the Pb-free (1 - x)BZT5-(x)BCT8 samples. The Raman spectroscopic data of the (1 - x)BZT5-(x)BCT8 compounds are shown in Figure 5. Evidently, the Raman study also supports the XRD results so as validate the crystal structure of all the samples. The observed Raman active modes and their corresponding peak

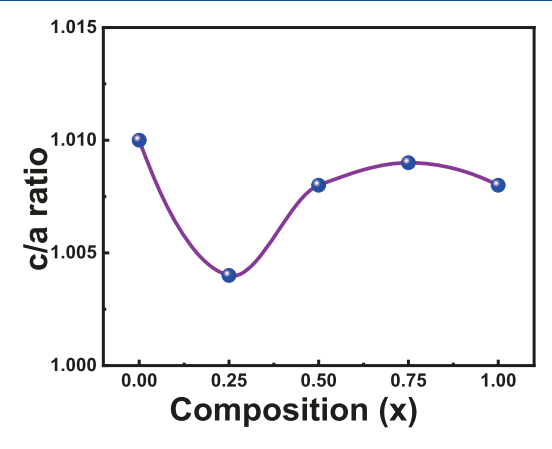


Figure 4. c/a ratio of (1 - x)BZT5-(x)BCT8 with (a) x = 0.00, (b) x = 0.25, (c) x = 0.50, (d) x = 0.75, and (e) x = 1.00.

positions are presented in Table 2. The absence of any other peaks (i.e., the peaks corresponding to the possible CaTiO₃ impurity phase) other than the expected ferroelectric phase of (1-x)BZT5-(x)BCT8 materials is an indication of the fact that the substitution of Ca²⁺ takes place for the Ba²⁺ site in the perovskite lattice. Further, from Figure 5, it is evident that the A₁(TO₂) mode observed at ~263 cm⁻¹ has the maximum scattering efficiency ^{66,67} and this peak is observed for all the samples. ²⁶

Figure 6 presents a comprehensive Raman spectroscopic study with temperature spanning from −193 to 227 °C for all the samples under investigation. The chosen temperature range is strategically significant, as it covers various critical structural transformations/transitions of the material. Transitions observed include the Rhombohedral to Orthorhombic (about -90 °C), Orthorhombic to Tetragonal (about 5 °C), and Tetragonal to Cubic (about 120 °C). By examining material across this broad temperature range (-193 to 227 °C), the investigation captures distinct structural alterations with the temperature. Raman spectroscopic analyses, within this temperature range, offer a valuable information on the vibrational and structural characteristics of the material, contributing to a comprehensive characterization of thermal response and phase evolution. Increase of temperature (from -193 to 227 °C) leads to decrease in intensity of the characteristic Raman peaks observed in the samples. These variations can be associated with modifications in the population of vibrational modes, crystal symmetry, or the

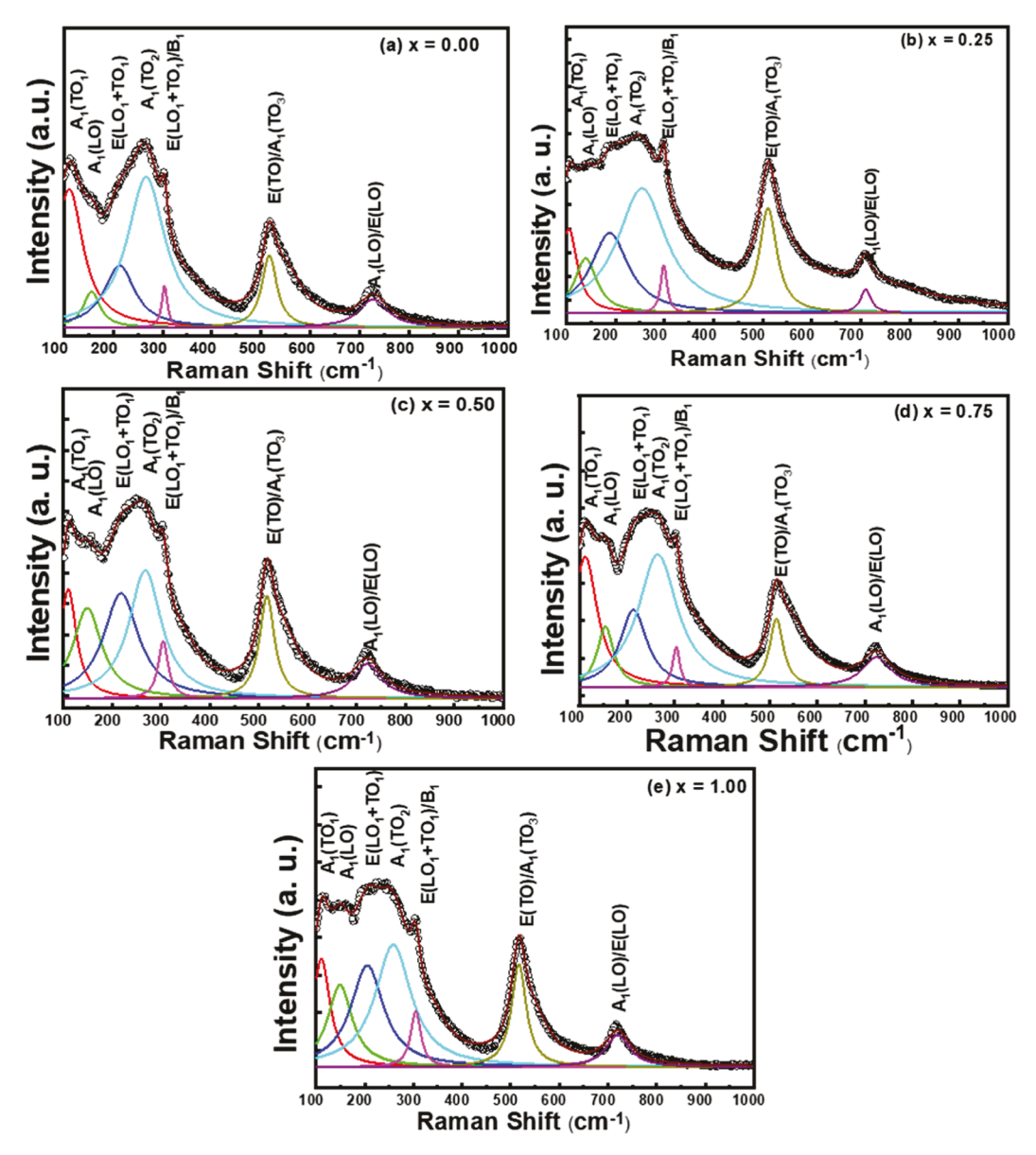


Figure 5. Raman spectra of (1 - x)BZT5 - (x)BCT8 with (a) x = 0.00, (b) x = 0.25, (c) x = 0.50, (d) x = 0.75, and (e) x = 1.00.

Table 2. Raman Modes and Peak Positions of (1 - x)BZT5-(x)BCT8 Compositions

	Raman modes with peak positions (cm ⁻¹)								
\boldsymbol{x}	$A_1(TO_1)$	$A_1(LO_1)$	$E(LO_1 + TO_1)$	$A(TO_2)$	$E(LO + TO)/B_1$	$E(TO)/A_1(TO_3)$	$A_1(LO)/E(LO)$		
0.00	112	156	211	263	303	516	723		
0.25	107	140	186	253	300	512	709		
0.50	112	147	218	267	304	516	720		
0.75	113	154	213	264	302	514	727		
1.00	110	148	204	257	305	516	721		

presence of certain structural defects. The intensity changes in specific bands offer valuable evidence about the thermal stability and structural evolution of the ceramics. Further, with increase in temperature, the width of Raman peaks is broadened and this broadening can be connected with the changes in crystal size, disorder, or thermal motion of atoms. These features provide insights into the material's phase transitions or structural transformations under different temperature conditions.

3.3. Morphology and Microstructure. To achieve a better piezoelectric response of the piezoelectric samples, the optimum grain size is crucial. Thus, to get information about microstructure of the samples, we have analyzed SEM images (Figure 7) of all the samples with variable composition. It is seen that all the (1 - x)BZT5-(x)BCT8 samples display a dense microstructure. It is seen in these images that the grain size increases up to x = 1.00 (BCT8). For samples with the composition of x = 0.50, x = 0.75, and x = 1.00, the grain growth is achieved without any pores. For the composition

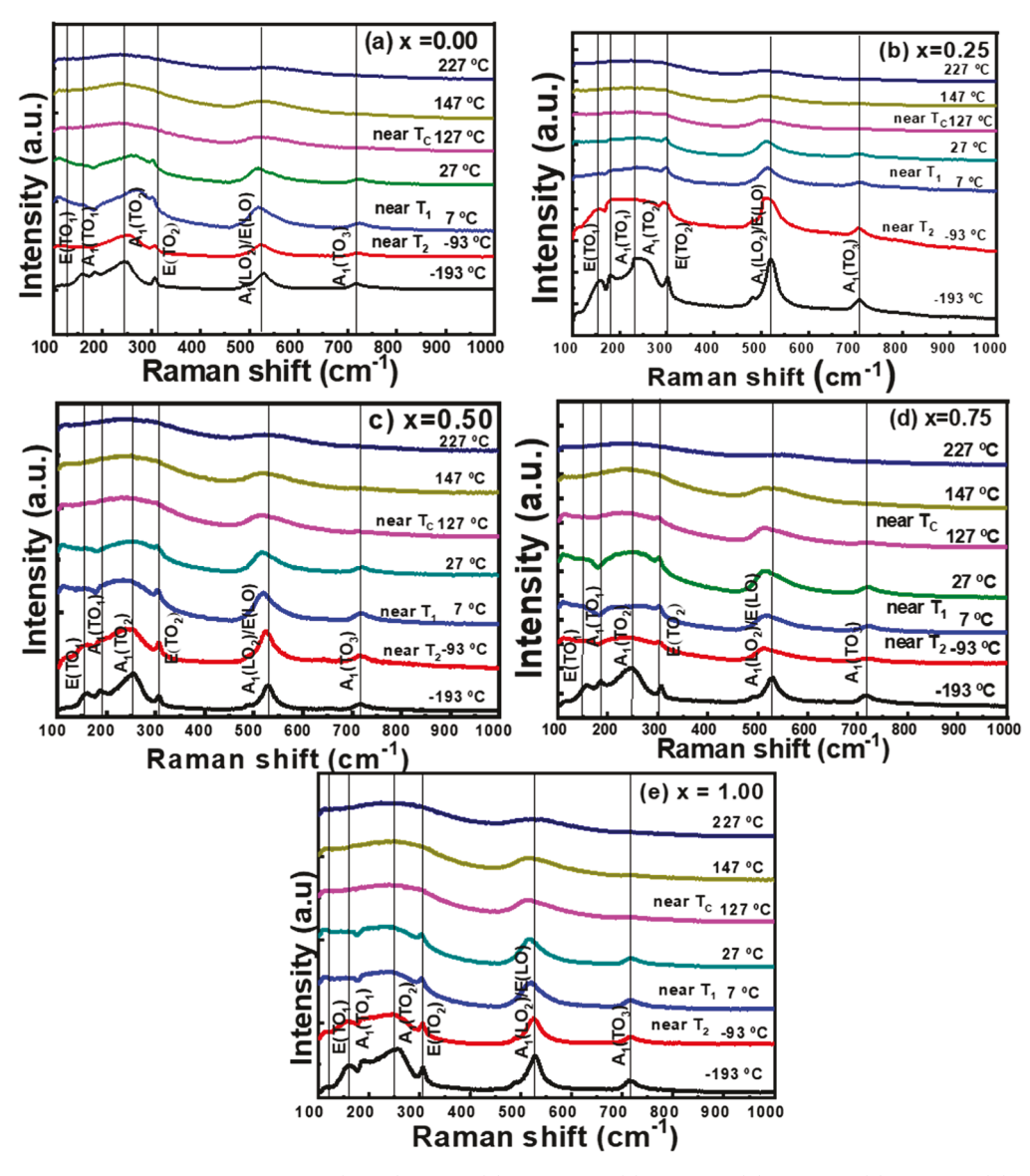


Figure 6. Temperature-dependent Raman spectra of (1 - x)BZTS - (x)BCT8 with (a) x = 0.00, (b) x = 0.25, (c) x = 0.50, (d) x = 0.75, and (e) x = 1.00.

with x = 0.00, the microstructure shows smaller grains among the ferroelectric samples. Thus, it is expected that the samples with x = 0.50, x = 0.75, and x = 1.00 may result in higher piezoelectric coefficients. Further, it is well-known that the density and pore size depend on the sintering temperature, which plays a key role in deciding the properties of the resulting materials. Densities of all the (1 - x)BZT5 - (x)BCT8 samples were measured using Archimedes' principle. The density values obtained are listed in Table 1. The sample with x = 0.00 shows the maximum density of 5.65 g/cm³ (96%), whereas the sample with x = 0.25 has the minimum density of 5.31 g/cm³ (90%).

The energy-dispersive X-ray spectra of the (1-x)BZT5-(x)BCT8 samples are shown in Figure S2. The EDS analyses can be used to validate the chemical homogeneity and elemental composition. Although these ceramic materials are complex in nature and contain multiple elements, the X-ray energy is the characteristic of the particular atom(s) that is/were involved in the production of the X-rays. ^{69,70} Hence, the X-rays and their respective energy positions can provide the

signature of the atoms present in the (1-x)BZT5-(x)BCT8 samples. The atomic and weight percentages of the specific elements present in (1-x)BZT5-(x)BCT8 are presented in Table 3. The EDS spectra analyses confirm and validate the chemical composition as well as chemical homogeneity of all the ferroelectric samples.

3.4. Dielectric Properties. Figure 8 shows the frequency response of the dielectric constant for all of the samples. The real part of the dielectric constant (ε') was calculated using the following equation. ^{71,72}

$$\varepsilon' = \frac{1129 \times C(\text{nF}) \times t(\text{mm})}{A(\text{cm}^2)}$$
 (5)

where ε' is the real part of the dielectric constant, C is the capacitance of materials in nano-Farad, t is the thickness of the sample in mm, and A is the area of the sample. Among all the samples with variable composition, x=1.00 attains the maximum value of dielectric constant ($\varepsilon'\approx 1416\ @\sim 0.8\ MHz$), whereas x=0.75 has the minimum value ($\varepsilon'=1000\ @\sim 0.8\ MHz$). A significant drop (Table 4) in dielectric constant

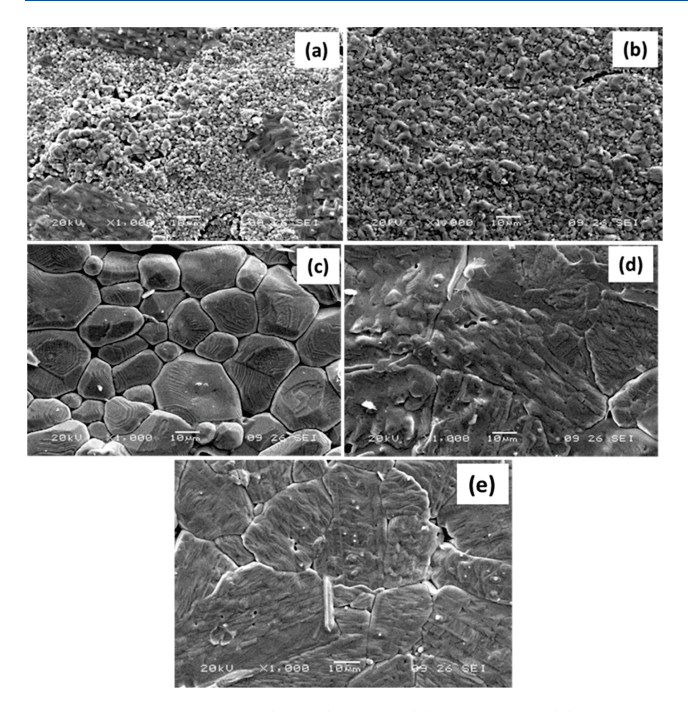


Figure 7. SEM images of (1 - x)BZT5 - (x)BCT8 with (a) x = 0.00, (b) x = 0.25, (c) x = 0.50, (d) x = 0.75, and (e) x = 1.00.

at \sim 0.8 MHz, compared to ε' at \sim 42 Hz, is observed except for the x=0.00 sample. There is about 7.6% lower drop in dielectric constant for x=0.00, whereas the maximum 30% drop in ε' was observed for the x=0.25 sample. Thus, it is expected from the observed dielectric response that there can be a prospect to retain a permanent dipole moment up to the frequency of \sim 0.8 MHz.

The dielectric dispersion of the samples exhibits the typical behavior. It is seen (Figure 8) that the dielectric constant decreases with the increasing frequency, i.e., all the samples show usual dielectric dispersion. From the dielectric measurements, it can be decided that the x=1.00 sample can be a suitable candidate for capacitor applications as it has a maximum value of the dielectric constant of 1444 at ~0.8 MHz. Specifically, the BCT8 sample is suitable for capacitor applications as it retains a high dielectric constant at a high frequency in the measured range.

Understanding of frequency-dependent dielectric properties provides valuable information about the dynamics of polarization and the material's response to the external electric fields. Dielectric loss, often associated with energy dissipation in the material, can exhibit frequency-dependent behavior. In Figure 9 (dielectric loss with changes in frequency), changes in frequency influence the dielectric response of the material, and thus all the samples show an increase in dielectric loss at higher frequencies. The observed variation in the dielectric loss with

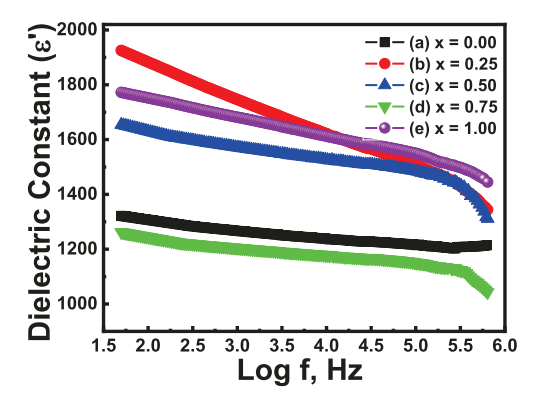


Figure 8. Dielectric constant with frequency of (1 - x)BZT5 - (x)BCT8 with (a) x = 0.00, (b) x = 0.25, (c) x = 0.50, (d) x = 0.75, and (e) x = 1.00.

Table 4. Dielectric Constant Values of (1 - x)BZT5-(x)BCT8 Compositions

x	dielectric constant (ε') (@42 Hz)	dielectric constant (@ ~0.8 MHz)	% drop in the dielectric constant (ε')
0.00	1318	1213	7.6
0.25	1927	1344	30.3
0.50	1650	1314	20.4
0.75	1264	1042	17.6
1.00	1761	1444	18

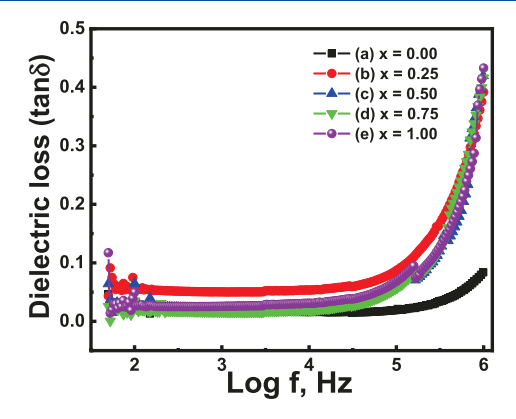


Figure 9. Dielectric loss ($\tan \delta$) with a frequency of (1 - x)BZT5 - (x)BCT8 with variable composition. The data shown are for x = 0.0 - 1.0.

changes in frequency can be attributed to the relaxation processes present in the samples. Especially, all the samples exhibit a lower and stable dielectric loss (up to 30 kHz) across the tested frequency range. The observed lower and stable dielectric behavior suggests that the materials maintain their dielectric properties within this frequency regime. The stable

Table 3. EDS Elemental Composition Analysis of (1 - x)BZT5-(x)BCT8

	x = 0.00		x = 0.25		x = 0.50		x = 0.75		x = 1.00	
element	wt %	atom %								
ОК	33.81	74.78	36.67	77.6	36.15	76.58	35.91	76.36	36.27	77
Ca K			0.24	0.13	0.63	0.53	0.92	0.78	0.24	0.2
Ti K	16.87	12.47	14.49	11.25	15.61	11.05	14.68	10.42	15.36	10.89
Zr L	0.31	0.12	0.26	0.4	0.74	0.27	3.36	1.25		
Ba L	49.01	12.63	48.34	10.63	46.87	11.57	45.13	11.18	48.13	11.91

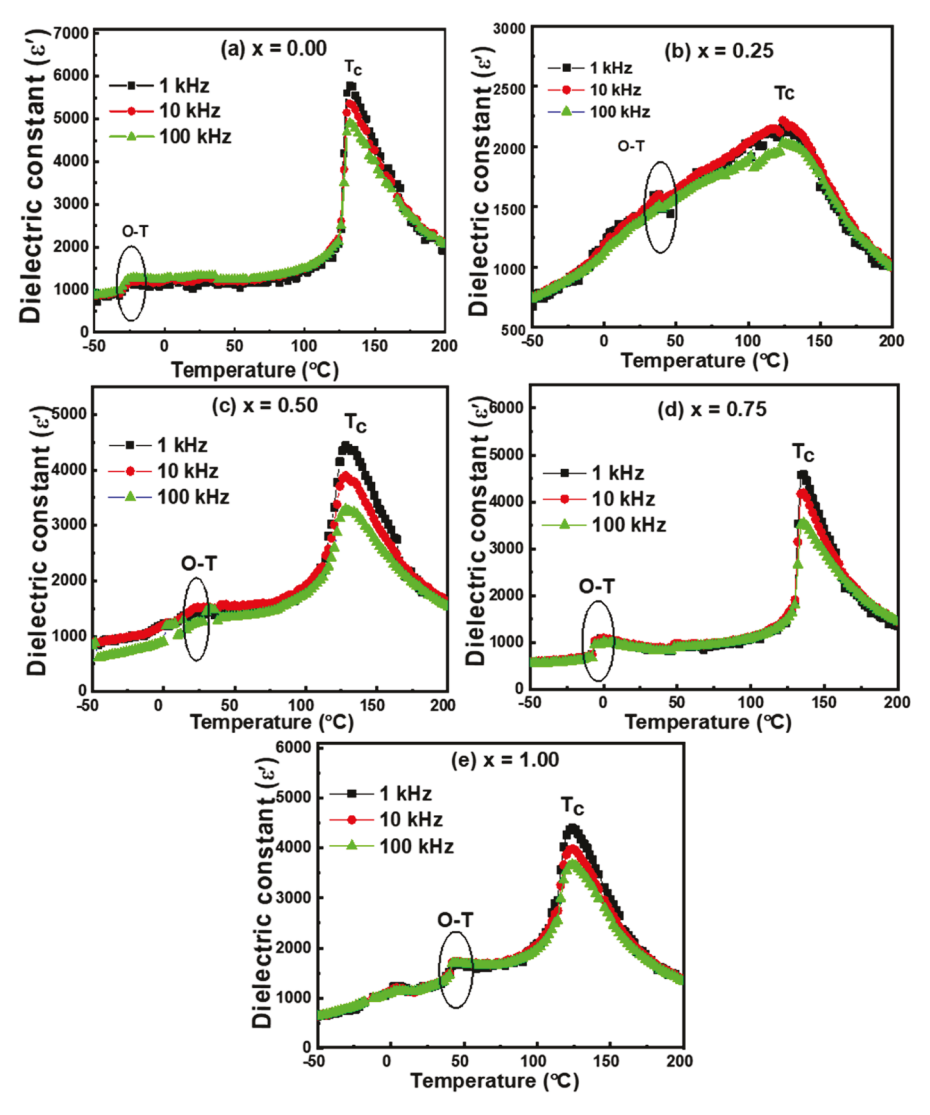


Figure 10. Dielectric constant with temperature (1 - x)BZTS-(x)BCT8 with (a) x = 0.00, (b) x = 0.25, (c) x = 0.50, (d) x = 0.75, and (e) x = 1.00.

dielectric constant with low loss is a desirable characteristic of materials intended for various applications, particularly in electronic devices, where reliable and uniform dielectric properties are crucial. Thus, the observed lower and stable dielectric loss up to 30 kHz indicates that the (1-x)BZT5-(x)BCT8 materials possess a consistent response to alternating electric fields within this frequency domain, highlighting their potential suitability for applications for reliable dielectric performance in this frequency range.

To investigate temperature-dependent phase transformation, the dielectric constant was measured for all the samples as a function of temperature (-50 to 200 °C) at three different frequencies, viz., 1, 10, and 100 kHz. The data are presented in Figure 10, where it is seen that the structural phase transitions are present for all the (1-x)BZT5-(x)BCT8 compositions. All the samples show transformation from an orthorhombic (O) phase to a tetragonal (T) phase and finally to a cubic phase as the temperature increases. Transition temperature and the corresponding dielectric constant values at different frequencies (1, 10, and 100 kHz) for all the (1-x)BZT5-(x)BCT8 compositions are presented in Table 5. The dielectric constant, also known as the relative permittivity, is a property that quantifies how well a material can store

Table 5. Transition Temperature $(T_{\rm trans})$ and the Corresponding Dielectric Constant (ε') Values at Different Frequencies (1, 10, and 100 kHz) along with Diffusivity Factors (γ) @ 10 kHz for (1-x)BZT5-(x)BCT8 Compositions

				ε' at T_{tran}	ıs	
\boldsymbol{x}	transition	$T_{\rm trans}$ (K)	1 kHz	10 kHz	100 kHz	γ @ 10 kHz
0.00	О-Т	247	1128	1150	1255	1.49
	$T_{\rm C}$	405	5779	5372	4903	
0.25	O-T	311	1597	1590	1501	1.51
	$T_{\rm C}$	397	2158	2217	2034	
0.50	O-T	295	1420	1510	1261	1.40
	$T_{\rm C}$	401	4446	3897	3311	
0.75	O-T	267	992	1034	949	1.23
	$T_{\rm C}$	407	4583	4216	3557	
1.00	O-T	315	1649	1724	1707	1.48
		396	4412	3986	3692	

electrical energy in an electric field. It is an essential parameter in understanding the behavior of dielectric materials, particularly in the context of their response to temperature variations.

In Figure 10, as the temperature rises from -50 °C, the dielectric constant of all ferroelectric compositions shows distinct variations. Initially, at lower temperatures (up to 50 °C), the materials display an orthorhombic phase. As the temperature gradually increases further, a transition occurs, and the materials possess a tetragonal structure. This alteration in the crystal structure corresponds to a significant increase in the dielectric constant. Also, with the increasing temperature, the ferroelectric compositions reach a critical point where another phase transition takes place and the materials enter a cubic phase. At this Curie temperature, the dielectric constant is observed to decrease with increase in temperature. These transitions are crucial for understanding and optimizing the performance of ferroelectric materials in various technological applications such as dielectric capacitors, ferroelectric devices, and sensors, where their dielectric properties play a significant role. Further investigation and analysis of these phase transitions can shed light on the underlying mechanisms driving the structural changes and the corresponding variations in the dielectric constant.

The composition-dependent dielectric constant at different frequencies (1, 10, 100, and 1 MHz) is measured at room temperature and shown in Figure 11. It is observed that the

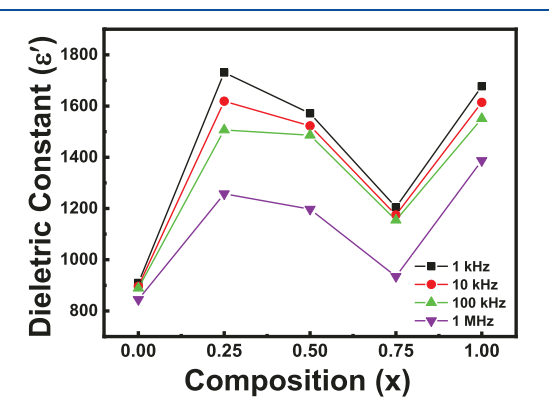


Figure 11. Frequency-dependent dielectric constant values of (1 - x)BZTS - (x)BCT8 at room temperature.

dielectric constant changes with frequency for all the samples. However, for the composition with x = 0.00, the change in dielectric constant is less compared to other compositions. To describe the diffusivity of a phase transition, a diffusivity factor (γ) is calculated using modified Curie–Weiss law given by ⁷⁶

$$\frac{1}{\varepsilon_{\rm r}} - \frac{1}{\varepsilon_{\rm m}} = \frac{(T - T_{\rm m})^{\gamma}}{C} \tag{6}$$

where γ and C are constants and $1 \le \gamma \le 2$. The diffusivity factor γ determines the type of the phase transition. For example, with $\gamma=1$, a normal Curie—Weiss law describes the phase transition; $\gamma=2$ gives a complete diffuse phase transition. The $\varepsilon_{\rm m}$ is the maximum value of dielectric permittivity and $T_{\rm m}$ is the corresponding temperature to the maximum value of dielectric permittivity. Accordingly, we have estimated the diffusivity factor from the graph of $\ln(1/\varepsilon_{\rm r}-1/\varepsilon_{\rm m})$ vs $\ln(T-T_{\rm m})$ at a 10 kHz frequency (Figure 12) for (1-x)BZT5—(x)BCT8 compositions. The values of diffusivity factors are listed in Table 5. A careful observation of the graph illustrates several important observations. First, the observed range of diffusivity factors from 1.23 to 1.51 indicates the varying degrees of particle mobility among the samples.

Samples exhibiting higher diffusivity factors signify greater particle mobility, suggesting faster and more efficient diffusion processes within that material. We expect that this information can be helpful for the development of materials with tailored diffusion properties for applications such as energy storage, catalysis, or transport phenomena.

3.5. Ferroelectric Properties. Ferroelectric measurements can predict the practicality of synthesized samples for data storage applications. The P-E measurements, which are shown in Figure 13, confirm the ferroelectric behavior of all the samples. From these P-E hysteresis loops, we have obtained the ferroelectric parameters, namely, the spontaneous polarization (P_s) , maximum polarization (P_{max}) , remnant polarization (P_r) , coercivity (E_c) , and the ratio (P_r/P_s) (Table 6). These parameters are plotted against the composition (Figure 14) in order to understand the effect of composition on potential applications. From Figure 14a, it is seen that the sample with x = 1.00 shows a higher value of remnant polarization as 11.22 μ C/cm², which is essential for retaining stored data for a long time. The sample x = 1.00 shows a higher value of coercivity ($E_c = 8.32 \text{ kV/cm}$), which is good for permanent memory (FeRAM) applications (Figure 14b). Among all the samples, the squareness ratio (P_r/P_s) is observed to be higher as ~ 0.70 for the x = 0.00 sample (Figure 14c). The coercive field (E_c) is expected to be smaller to reduce energy consumption (i.e., area enclosed by P-E hysteresis loop) during writing the data and it is expected to be higher so that the written data should not be altered by keeping electronic components in close vicinity of external electric field. The sample with x = 1.00 has low coercivity, which may be suitable for volatile or random-access memory applications.

3.6. Current Density (J-E) Plots. The current density (J, μ A/cm²) measurements with an electric field for all ferroelectric samples are given in Figure 15. The maximum values of the current density obtained from the J-E plots are tabulated in Table 6. The presence of a higher value of current density represents that the samples are useful for strain sensors and even for detecting human motion applications. ⁸⁰ Among all the samples, the x = 1.00 sample shows the maximum value current density (123.0 μ A/cm²), whereas the x = 0.25 sample shows the minimum value (17.8 μ A/cm²). The sharp peaks in J-E plots signifies fully saturated ferroelectric P-E hysteresis loops, ⁸¹ except for x = 0.25.

3.7. Electrostriction Study. Figure 16 illustrates the electrostriction measurements, specifically showing the relationship between strain and polarization for the set of (1 - x) BZT5–(x)BCT8 compositions. The electrostrictive coefficient (Q) is then calculated from these graphs using the following equation⁸²

$$Q = \frac{S}{P^2} \tag{7}$$

where Q is the electrostrictive coefficient, S represents the strain, and P denotes the polarization. Table 6 provides a comprehensive overview of the electrostrictive coefficient (Q) values for all of the samples. From Table 6, it seen that the material with the x=0.00 composition achieves the highest electrostrictive coefficient value, as $4.13 \times 10^{-4} \, (\text{cm}^2/\mu\text{C})^2$. This observation implies that the sample with x=0.00 exhibits a superior electrostrictive performance, making it potentially more suitable for applications in electromechanical actuators. 39,83,84 Further, the electrostrictive coefficient is a crucial

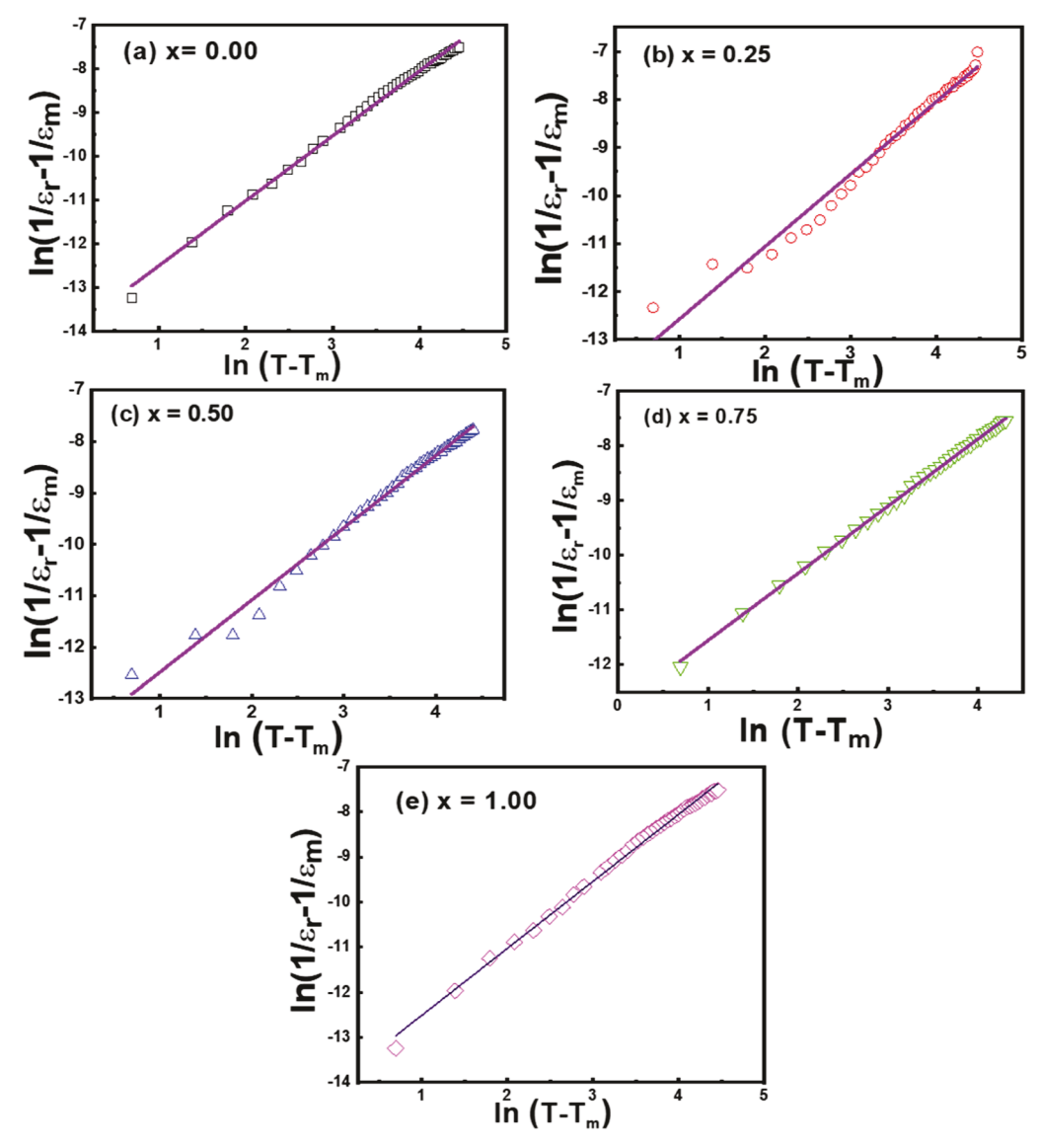


Figure 12. Plots of $\ln(1/\varepsilon_{\rm r}-1/\varepsilon_{\rm m})$ vs $\ln(T-T_{\rm m})$ at a 10 kHz frequency for (1-x)BZT5-(x)BCT8.

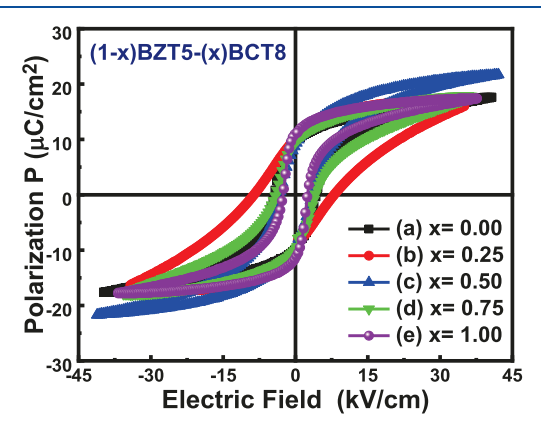


Figure 13. P-E hysteresis loop of (1-x)BZTS-(x)BCT8 with (a) x=0.00, (b) x=0.25, (c) x=0.50, (d) x=0.75, and (e) x=1.00 compositions.

parameter in electromechanical systems, and a higher value indicates a more significant strain response to an applied electric field, highlighting the material's efficiency in converting electrical energy into mechanical motion.

3.8. Piezoelectric Properties. The strain (S-E) plots, as depicted in Figure 17, offer a dynamic visual representation of the piezoelectric materials' response to an electric field applied. The strain (S) is directly influenced by the electric field (E), leading to changes in dimensions of the materials. This relationship is quantified by the equation⁸⁵

$$(S_3 = d_{33}^* \times E_3) \tag{8}$$

where the numerals 1, 2, and 3 correspond to the X, Y, and Z axes, respectively. In this context, S_3 represents the maximum strain along the Z-axis, d_{33}^* is the converse piezoelectric coefficient (reflecting the coupling of an electric field applied along the Z-axis with the resulting strain along the same axis), and E_3 is the maximum applied external electric field along the Z-axis. The calculated converse piezoelectric coefficient (d_{33}^*) values are presented in Table 7, revealing that the composition with x=0.50 exhibits a maximum strain of approximately 0.179%, making it particularly advantageous for transducer applications. Furthermore, this composition demonstrates the highest converse piezoelectric coefficient of \sim 430 pm/V, attributed to the motion of ferroelectric domains.

Table 6. Ferroelectric and Piezoelectric Parameters of (1 - x)BZT5-(x)BCT8 Compositions

x	$\frac{P_{\rm r}}{(\mu{\rm C/cm}^2)}$	$P_{\rm max} (\mu { m C/cm}^2)$	spontaneous polarization, P_s $(\mu \text{C/cm}^2)$	$\frac{E_{\rm c}}{({\rm kV/cm})}$	$\frac{E_{\rm max}}{({\rm kV/cm})}$	squareness ratio, $P_{\rm r}/P_{\rm s}$	strain, S (%)	maximum current density, $J(\mu A/cm^2)$	electrostrictive coefficient, $Q = S/P^2 (cm^2/\mu C)^2$
0.00	9.76	17.61	13.98	4.39	40.7	0.70	0.128	68.4	4.13×10^{-4}
0.25	10.51	16.24	16.20	8.32	34.9	0.65	0.092	17.8	3.89×10^{-4}
0.50	9.18	21.71	18.78	3.35	42.1	0.49	0.179	60.2	3.50×10^{-4}
0.75	9.72	17.86	16.20	4.10	36.5	0.60	0.110	47.7	3.81×10^{-4}
1.00	11.22	17.61	16.86	2.54	37.6	0.67	0.121	123.0	3.45×10^{-4}

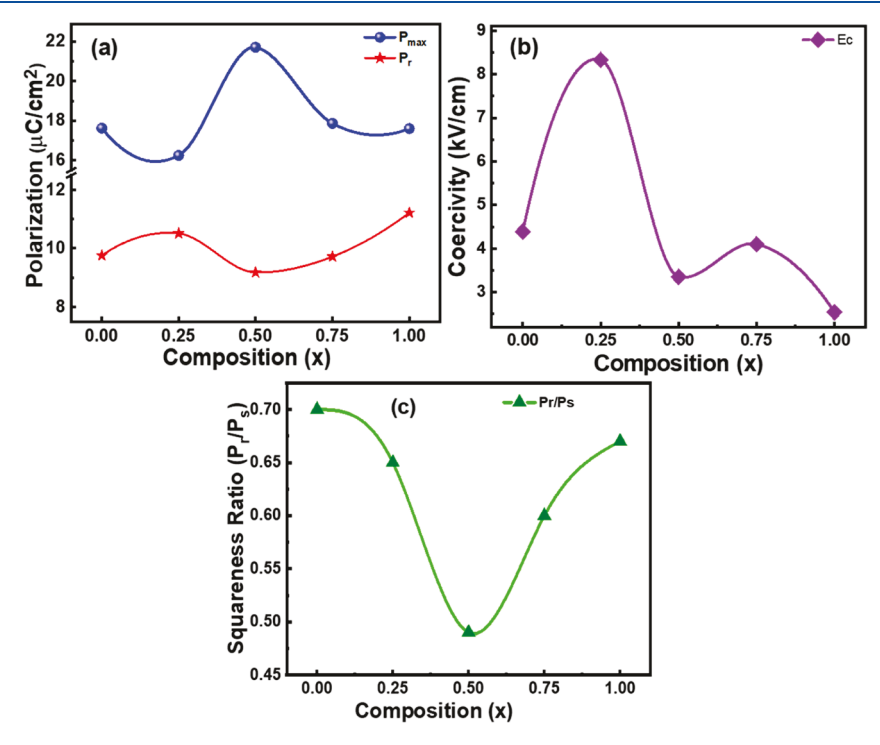


Figure 14. Ferroelectric parameters. (a) Remanence and maximum polarization. (b) Coercivity (E_c) . (c) Squareness ratio (P_r/P_s) .

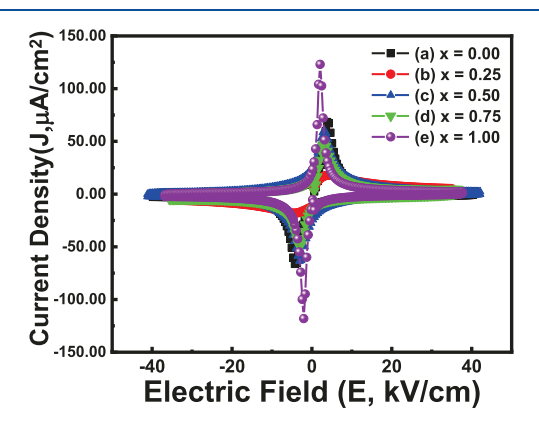


Figure 15. Current density (*J*) versus electric field (*E*) of (1 - x)BZT5 - (x)BCT8 with (a) x = 0.00, (b) x = 0.25, (c) x = 0.50, (d) x = 0.75, and (e) x = 1.00.

presence of the symmetric S-E loops for all ferroelectric samples highlights the significance of the strain plots, which is essential for actuator applications.⁸⁸

The inclusive relation extends to the complete exploration of piezoelectric properties, specifically the piezoelectric coefficient (d_{33}) , discussed in the subsequent sections. The piezoelectric coefficient (d_{33}) values are calculated (see Table 7) using the following equation:⁸⁹

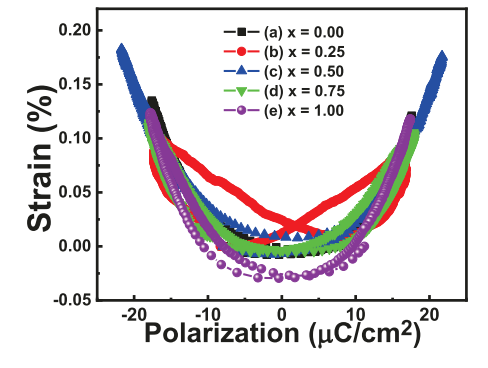


Figure 16. Strain versus polarization curves of (1 - x)BZT5-(x)BCT8 with (a) x = 0.00, (b) x = 0.25, (c) x = 0.50, (d) x = 0.75, and (e) x = 1.00.

$$d_{33} = 2Q\varepsilon'\varepsilon_0 P_{\rm s} \tag{9}$$

where Q is the electrostrictive coefficient, ε' is the real part of the dielectric constant, ε_0 is the permittivity of free space, and P_s is the spontaneous polarization. It is seen from Table 7 that the composition with x=0.50 emerges as the most suitable material, as it shows the highest piezoelectric coefficient value of 199 pC/N. This emphasizes its significant role in applications requiring efficient conversion of mechanical stress to electrical voltage. We expect that the observed grain size (20

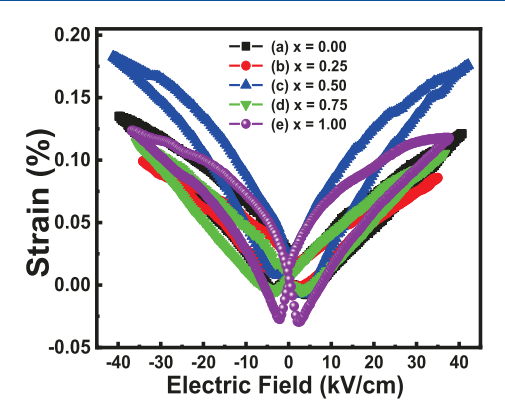


Figure 17. S-E curves of (1-x)BZT5-(x)BCT8 with (a) x = 0.00, (b) x = 0.25, (c) x = 0.50, (d) x = 0.75, and (e) x = 1.00.

Table 7. Piezoelectric Coefficient, Grain Size, and Density Values of (1 - x)BZT5 - (x)BCT8 Compositions

		d_{33} (pC/N)		
x	d ₃₃ * (pm/V)	theoretical	experimental	average grain size (μm)	Archimedes density (g/cm ³)
0.00	318 ± 1	94 ± 1	140 ± 1	1.5	5.65
0.25	267 ± 1	169 ± 1	219 ± 1	4	5.31
0.50	430 ± 1	199 ± 1	360 ± 1	20	5.47
0.75	304 ± 1	119 ± 1	190 ± 1	50	5.37
1.00	324 ± 1	193 ± 1	160 ± 1	40	5.57

 μ m) plays an important role in enhancing the piezoelectric (d_{33} value) properties for the x=0.50 composition. The comprehensive data presented in Figure 17, Table 7, and subsequent discussions highlight the inclusive relationship between strain (S-E) plots and piezoelectric properties. Thus, on overall observation of the measured piezoelectric properties, we predict that the x=0.50 sample can be a suitable candidate as a lead-free material with exceptional performance in transducer and piezoelectric applications.

However, x = 0.00 exhibits a minimum value of 94 pC/N. This may be due to a reduced grain size. The piezoelectric properties of ferroelectric ceramics are highly dependent on the grain size, internal stress, poling electric field strength, and the degree of ferroelectric domain switching. 90 From the converse piezoelectric coefficient (d_{33}^*) values (Table 7), it is evident that the sample x = 0.50 may be more suitable for piezoelectric sensor and actuator applications. Furthermore, piezoelectric coefficient values are higher for the x = 0.50sample having a grain size of 20 μ m. Also, for x = 1.00, the grain size is 40 μ m and piezoelectric constant is 190 pC/N. If the grain size is smaller (1.5 μ m for x = 0.00) or more (50 μ m for x = 1.00), then the piezoelectric coefficient values are observed to be decreasing. Thus, a dense ferroelectric sample with optimum grain size is essential to attain higher value of piezoelectric coefficients. 79,91

The piezoelectric constant, a key parameter characterizing the piezoelectric properties of materials, provides a measure of their ability to convert mechanical stress into electrical voltage and vice versa. In this context, the piezoelectric constants were measured for all of the ferroelectric materials (1 - x)BZT5 - (x)BCT8 with varying composition. For x = 0.00, the piezoelectric constant is 94 pC/N. This value indicates a moderate piezoelectric response for this composition, suggesting that it may possess some piezoelectric capabilities but with

a relatively lower magnitude compared to the other samples. However, for x = 0.25, the piezoelectric constant significantly increases to 169 pC/N. This observation suggests that with the increase of the Ca^{2+} content, for Ba^{2+} in the (1-x)BZT5-(x)BCT8 composition, it enhances the piezoelectric response considerably, leading to a higher ability to generate electric voltage under mechanical stress. As x increases to 0.50, the piezoelectric constant reaches its maximum value of 199 pC/ N. This composition validates the highest piezoelectric response among the samples investigated, indicating its exceptional ability to convert mechanical energy into electrical voltage. Such materials are highly authoritative for various applications including sensors, actuators, and energy-harvesting devices. For x = 0.75, the piezoelectric constant decreases to 119 pC/N, which is lower than the maximum value, but still it retains a significant piezoelectric response. Finally, for x = 1.00, the piezoelectric constant obtained is 193 pC/N. This value indicates a substantial recovery in the piezoelectric response compared to the x = 0.75 composition, suggesting that the pure BCT8 composition maintains its piezoelectric characteristics effectively. A comparative data of piezoelectric coefficients (d_{33}) measured for the ferroelectric materials in the present study and the materials studied in the literature is given in Table 8. The measured piezoelectric coefficients for

Table 8. Comparison of the Piezoelectric Coefficient Values of Ferroelectric Samples with the Literature

composition	piezoelectric coefficient (d_{33}) (pC/N)
x = 0.00 (present study)	140
x = 0.25 (present study)	219
x = 0.50 (present study)	360
x = 0.75 (present study)	190
x = 1.00 (present study)	160
Mo/Cr-doped CaBi ₂ Nb ₂ O ₉ ⁹⁰	15
LiSbO ₃ -(Na _{0.5} K _{0.5})NbO ₃ ⁹⁰	143
BNLKT4-28 ⁹¹	135
BNT-0.3 ⁹²	92
BZT-Portland cement ⁹³	10
CT ⁹⁴	130
BZT-BCT ⁹⁵	600
BT-based systems ⁹⁶	150

the (1-x)BZT5-(x)BCT8 samples provide an important insight into the effect of composition variation on the piezoelectric properties. This information can be crucial for researchers and engineers seeking to tailor materials with specific piezoelectric characteristics for diverse applications in areas such as robotics, energy harvesting, and medical devices. $^{96-98}$

4. SUMMARY AND CONCLUSIONS

Tetravalent Zr^{4+} and divalent Ca^{2+} substituted for Ti^{4+} and Ba^{2+} in $BaTiO_3$ lead-free ceramic compositions, (1-x)BZT5-(x)BCT8 where $x=0.00,\ 0.25,\ 0.50,\ 0.75,\ and 1.00$ (where BZT5 is $BaZr_{0.05}Ti_{0.95}O_3$ and BCT8 is $Ba_{0.92}Ca_{0.08}TiO_3$), were synthesized by the standard ceramic method. A structural study using Rietveld refinement of all of the compositions confirms the presence of tetragonal and orthorhombic phases in all compositions. The microstructural analyses using SEM specify that the maximum grain growth is observed for the x=0.75 sample. The average grain size increases with an increase in the concentration of the BCT8

phase from 1.5 μ m (for the x=0.00 sample) to 50 μ m (for x=0.75 sample). The squareness ratio ($P_{\rm r}/P_{\rm s}$) is higher ($P_{\rm r}/P_{\rm s}=0.70$) for the x=0.00 sample and the moderate value of coercivity ($E_{\rm c}=4.39$ kV/cm) is good for permanent memory device applications. The current density plots indicate that the x=1.00 sample can hold the maximum electric field and it also has the highest value of current density, 123.0 μ A/cm². Strain measurements show that the x=0.50 and x=1.00 samples may be useful for electromechanical transducer applications. The Q-factor has the highest value (4.13 \times 10⁻⁴ (cm²/ μ C)²) for the x=0.00 sample, and thus, it is suitable for electromechanical applications. Thus, we conclude that the synthesized lead-free materials, with improved properties and performance, are useful for a variety of electronic device applications.

ASSOCIATED CONTENT

Supporting Information

The Supporting Information is available free of charge at https://pubs.acs.org/doi/10.1021/acs.jpcc.3c06914.

Additional details of synthesis of materials and chemical composition (EDS) data for (1 - x)BZT5-(x)BCT8 compounds (PDF)

AUTHOR INFORMATION

Corresponding Authors

Yesh D. Kolekar — Department of Physics, Savitribai Phule Pune University, Pune 411007 Maharashtra, India; orcid.org/0000-0002-9466-3184; Phone: +91-20-2569-2678; Email: ydkolekar@gmail.com; Fax: +91-20-2569-1684

C. V. Ramana — Center for Advanced Materials Research (CMR) and Department of Aerospace and Mechanical Engineering, University of Texas at El Paso, El Paso, Texas 79968, United States; orcid.org/0000-0002-5286-3065; Email: rvchintalapalle@utep.edu

Authors

Swati K. Gaikwad – Department of Physics, Savitribai Phule Pune University, Pune 411007 Maharashtra, India; Department of Physics, Fergusson College (Autonomous), Pune 411004 Maharashtra, India

Shahaji P. Kharat – Department of Physics, Savitribai Phule Pune University, Pune 411007 Maharashtra, India; Department of Physics, Fergusson College (Autonomous), Pune 411004 Maharashtra, India

Bharat G. Baraskar – Department of Physics, Savitribai Phule Pune University, Pune 411007 Maharashtra, India

Paul G. Nalam — Center for Advanced Materials Research (CMR), University of Texas at El Paso, El Paso, Texas 79968, United States; orcid.org/0000-0001-7653-228X

Ajit R. James – Ceramics and Composites Group, Defence Metallurgical Research Laboratory, (Ministry of Defence), Hyderabad 500058 Telangana, India

Complete contact information is available at: https://pubs.acs.org/10.1021/acs.jpcc.3c06914

Notes

The authors declare no competing financial interest.

ACKNOWLEDGMENTS

The authors are thankful to the Department of Science and Technology (Government of India), New Delhi, for providing financial assistance (ref. SR/FTP/PS-040/2010) to carry out the research work. Swati K. Gaikwad acknowledge the financial assistance from University Grant Commission for Basic Scientific Research (UGC-BSR) and DST-PURSE fellowships. The authors at the University of Texas at El Paso acknowledge, with pleasure, the support from the National Science Foundation (NSF) with NSF-PREM grant #DMR-1827745.

REFERENCES

- (1) Kharat, S. P.; Gaikwad, S. K.; Nalam, P. G.; Kambale, R. C.; James, A. R.; Kolekar, Y. D.; Ramana, C. V. Effect of crystal structure and phase on the dielectric, ferroelectric, and piezoelectric properties of Ca²⁺- and Zr⁴⁺-substituted barium titanate. *Cryst. Growth Des.* **2022**, 22 (9), 5571–5581.
- (2) Kumar, D.; Rout, S. K. Significantly enhanced energy storage density and efficiency at low electric fields in lead-free Bi_{0.5}Na_{0.25}K_{0.25}TiO₃-K_{0.5}Na_{0.5}NbO₃ piezoceramics. ACS Appl. Electron. Mater. 2023, 5 (8), 4363–4376.
- (3) Li, J.; Chang, Y.; Yang, S.; Tian, Y.; Hu, Q.; Zhuang, Y.; Xu, Z.; Li, F. Lead-free bilayer thick films with giant electrocaloric effect near room temperature. ACS Appl. Mater. Interfaces 2019, 11 (26), 23346—23352.
- (4) Li, M.; Zhu, M.; Wei, Q.; Zhang, M.; Zheng, M.; Hou, Y.; Zhu, L.; Li, Y.; Hao, X. Achieving large electrocaloric effect in a wide temperature span for $(Na_{1/2}Bi_{1/2})TiO_3$ -based ceramics via the synergic effect of A-site vacancies and B-site complex cations. ACS Appl. Electron. Mater. **2021**, 3 (11), 5023–5030.
- (5) Jaffe, B.; Cook, W. R.; JR; Jaffe, H. Piezoelectric ceramics; Elsevier, 1971; pp 135–183.
- (6) Uchino, K. Chapter 7. Ferroelectric devices; Boca Raton, 2010.
- (7) Collin, M. S.; Venkatraman, S. K.; Vijayakumar, N.; Kanimozhi, V.; Arbaaz, S. M.; Stacey, R. G. S.; Anusha, J.; Choudhary, R.; Lvov, V.; Tovar, G. I.; et al. Bioaccumulation of lead (Pb) and its effects on human: A review. *J. Hazard. Mater. Adv.* **2022**, 100064.
- (8) Srianujata, S. Lead-the toxic metal to stay with human. *J. Toxicol. Sci.* 1998, 23 (SupplementII), 237–240.
- (9) Alengebawy, A.; Abdelkhalek, S. T.; Qureshi, S. R.; Wang, M. Q. heavy metals and pesticides toxicity in agricultural soil and plants: Ecological risks and human health implications. *Toxics* **2021**, *9* (3), 42
- (10) Anubhav, S.; Anuj, S.; Rohit, K. V.; Rushikesh, L. C.; Pritam, P. P.; Varad, N.; Vinay, A.; Sumit, K. C.; Garima, A.; Kumud, K. A.; et al. In *Heavy metal contamination of water and their toxic effect on living organisms*. *In The Toxicity of Environmental Pollutants*; Daniel Junqueira, D., Danielle Palma de, O., Eds.; Intech Open: Rijeka, 2022; Ch. 2, pp 1–19.
- (11) Muduli, S. P.; Lipsa, L.; Choudhary, A.; Rajput, S.; Parida, S. Modulation of electrical characteristics of polymer-ceramic graphene hybrid composite for piezoelectric energy harvesting. *ACS Appl. Electron. Mater.* **2023**, *5* (6), 3023–3037.
- (12) Reyes-Montero, A.; Rubio-Marcos, F.; Fuentes-Cobas, L. E.; Del Campo, A.; Castañeda-Guzmán, R.; Villafuerte-Castrejón, M. E.; Pardo, L. Confocal Raman microscopy, synchrotron x-ray diffraction, and photoacoustic study of Ba_{0.85}Ca_{0.15}Ti_{0.90}Zr_{0.10}O₃: Understanding structural and microstructural response to the electric field. *ACS Appl. Electron. Mater.* **2021**, *3* (7), 2966–2976.
- (13) Tripathy, A.; Saravanakumar, B.; Mohanty, S.; Nayak, S. K.; Ramadoss, A. Comprehensive review on flexoelectric energy harvesting technology: Mechanisms, device configurations, and potential applications. *ACS Appl. Electron. Mater.* **2021**, 3 (7), 2898–2924.
- (14) Barzilay, M.; Elangovan, H.; Ivry, Y. Surface nucleation of the paraelectric phase in ferroelectric BaTiO₃: Atomic scale mapping. ACS Appl. Electron. Mater. **2019**, *1* (11), 2431–2436.

- (15) Ben Ayed, A.; Bouhamed, A.; Nouri, H.; Abdelmoula, N.; Khemakhem, H.; Kanoun, O. Robust and flexible piezoelectric lead-free Zn-BCZT/PVDF-HFP nanogenerators for wearable energy harvesting. ACS Appl. Electron. Mater. 2023, 5 (8), 4282–4295.
- (16) Khosla, R.; Sharma, S. K. Integration of ferroelectric materials: an ultimate solution for next-generation computing and storage devices. ACS Appl. Electron. Mater. 2021, 3 (7), 2862–2897.
- (17) Kharat, S. P.; Gaikwad, S. K.; Kambale, R. C.; Kolekar, Y. D.; Ramana, C. V. Correlation between cation distribution and magnetic and dielectric properties of Dy³⁺-substituted Fe-rich cobalt ferrite. *Inorg. Chem.* **2022**, *61* (48), 19319–19332.
- (18) Kharat, S. P.; Gaikwad, S. K.; Baraskar, B. G.; Das, D.; Kambale, R. C.; Kolekar, Y. D.; Ramana, C. V. Enhanced magnetoelectric effect in lead-free piezoelectric BaZr_{0.2}Ti_{0.8}O₃-0.5Ba_{0.7}Ca_{0.3}TiO₃ and Fe-rich magnetostrictive Co_{0.8}Fe_{2.2-x}Dy_xO₄ nanocomposites for energy harvesting applications. *Mater. Sci. Eng., B* **2023**, 116363.
- (19) Saito, Y.; Takao, H.; Tani, T.; Nonoyama, T.; Takatori, K.; Homma, T.; Nagaya, T.; Nakamura, M. Lead-free piezoceramics. *Nature* **2004**, *432*, 84–87.
- (20) Zhao, C.; Wu, H.; Li, F.; Cai, Y.; Zhang, Y.; Song, D.; Wu, J.; Lyu, X.; Yin, J.; Xiao, D.; Zhu, J.; Pennycook, S. J. Practical high piezoelectricity in barium titanate ceramics utilizing multiphase convergence with broad structural flexibility. *J. Am. Chem. Soc.* 2018, 140 (45), 15252–15260.
- (21) Liu, W.; Ren, X. Large piezoelectric effect in Pb-free ceramics. *Phys. Rev. Lett.* **2009**, 103 (25), 257602.
- (22) Baraskar, B. G.; Kolekar, Y. D.; Thombare, B. R.; James, A. R.; Kambale, R. C.; Ramana, C. V. Enhanced piezoelectric, ferroelectric, and electrostrictive properties of lead-free (1-x)BCZT-(x)BCST electroceramics with energy harvesting capability. *Small* **2023**, *19* (37), 2300549.
- (23) Tian, Y.; Chao, X.; Jin, L.; Wei, L.; Liang, P.; Yang, Z. Polymorphic structure evolution and large piezoelectric response of lead-free (Ba,Ca)(Zr,Ti)O₃ ceramics. *Appl. Phys. Lett.* **2014**, *104* (11), 192901
- (24) Jayakrishnan, A. R.; Karthik Yadav, P. V.; Silva, J. P. B.; Sekhar, K. C. Microstructure tailoring for enhancing the energy storage performance of $0.98[0.6Ba(Zr_{0.2}Ti_{0.8})O_3-0.4(Ba_{0.7}Ca_{0.3})TiO_3]-0.02BiZn_{1/2}Ti_{1/2}O_3$ ceramic capacitors. *J. Sci.: Adv. Mater. Devices* **2020**, *5* (1), 119–124.
- (25) Yang, Y.; Wang, W.; Chen, X.; Wang, Y.; Gao, D.; Xue, D. Enhanced thermal stability of lead-free $(1-x)Ba(Zr_{0.2}Ti_{0.8})O_3$ -x- $(Ba_{0.7}Ca_{0.3})TiO_3$ ferroelectric ceramics. *J. Mater. Sci.* **2020**, *55* (36), 16890–16899.
- (26) Parhi, C. C.; Thirumalasetty, A. B.; James, A. R.; Wuppulluri, M. Relative Investigation on Microwave-Assisted Zr-Modified PbTiO₃ and BaTiO₃ Ferroelectric Ceramics for Energy Storage Application. *ACS Omega* **2023**, *8* (41), 37752–37768.
- (27) Du, J.; Qiu, L.; Yang, C.; Chen, Y.; Zhu, K.; Wang, L. Effect of Different Ca²⁺ and Zr⁴⁺ Contents on Microstructure and Electrical Properties of (Ba,Ca)(Zr,Ti)O₃ Lead-Free Piezoelectric Ceramics. *Crystals* **2022**, *12* (7), 896.
- (28) Yoon, M. S.; Ur, S. C. Effects of A-site Ca and B-site Zr substitution on dielectric properties and microstructure in tin-doped BaTiO₃-CaTiO₃ composites. *Ceram. Int.* **2008**, *34* (8), 1941–1948.
- (29) Wu, J. BaTiO₃-Based Piezoelectric Materials. In Advances in Lead-Free Piezoelectric Materials; Springer Singapore: Singapore, 2018; pp 247–299.
- (30) Acosta, M.; Novak, N.; Rojas, V.; Patel, S.; Vaish, R.; Koruza, J.; Rossetti, G. A.; Rödel, J. BaTiO₃-based piezoelectrics: Fundamentals, current status, and perspectives. *Appl. Phys. Rev.* **2017**, *4*, 041305.
- (31) Puli, V. S.; Pradhan, D. K.; Adireddy, S.; Martinez, R.; Silwal, P.; Scott, J. F.; Ramana, C. V.; Chrisey, D. B.; Katiyar, R. S. Nanoscale polarisation switching and leakage currents in $(Ba_{0.955}Ca_{0.045})$ - $(Zr_{0.17}Ti_{0.83})O_3$ epitaxial thin films. *J. Appl. Phys. D.: Appl. Phys.* **2015**, *48*, 355502.
- (32) Keswani, B. C.; Saraf, D.; Patil, S. I.; Kshirsagar, A.; James, A. R.; Kolekar, Y. D.; Ramana, C. V. Role of A-site Ca and B-site Zr substitution in $BaTiO_3$ lead-free compounds: Combined experimental

- and first principles density functional theoretical studies. *J. Appl. Phys.* **2018**, *123* (20), 204104.
- (33) Jonker, G. H.; Kwestroo, W. The Ternary Systems BaO-TiO₂-SnO₂ and BaO-TiO₂-ZrO₂. *J. Am. Ceram. Soc.* **1958**, 41 (10), 390–394
- (34) Yu, Z.; Ang, C.; Guo, R.; Bhalla, A. S. Piezoelectric and strain properties of $Ba(Ti_{1-x}Zr_x)O_3$ ceramics. *J. Appl. Phys.* **2002**, *92*, 1489–1493.
- (35) Yasuda, N.; Hidehiro Ohwa, H. O.; Shigeto Asano, S. A. Dielectric properties and phase transitions of $Ba(Ti_{1-x}Sn_x)O_3$ solid solution. *Jpn. J. Appl. Phys.* **1996**, *35*, 5099–5103.
- (36) Fu, J.; Hou, Y.; Zheng, M.; Zhu, M. Topochemical conversion of (111) BaTiO₃ piezoelectric microplatelets using $Ba_6Ti_{17}O_{40}$ as the precursor. *Cryst. Growth Des.* **2019**, *19*, 1198–1205.
- (37) Maxim, F.; Ferreira, P.; Vilarinho, P. M.; Aimable, A.; Bowen, P. Additive-assisted aqueous synthesis of BaTiO₃ nanopowders. *Cryst. Growth Des.* **2010**, *10*, 3996–4004.
- (38) Panda, P. K. Review: environmental friendly lead-free piezoelectric materials. *J. Mater. Sci.* **2009**, *44*, 5049–5062.
- (39) Rödel, J.; Jo, W.; Seifert, K. T. P.; Anton, E. M.; Granzow, T.; Damjanovic, D. Perspective on the development of lead-free piezoceramics. *J. Am. Ceram. Soc.* **2009**, *92*, 1153–1177.
- (40) Feng, Y.; Li, W. L.; Xu, D.; Qiao, Y. L.; Yu, Y.; Zhao, Y.; Fei, W. D. Defect engineering of lead-free piezoelectrics with high piezoelectric properties and temperature stability. *ACS Appl. Mater. Interfaces* **2016**, *8* (14), 9231–9241.
- (41) Jian, X. D.; Lu, B.; Li, D. D.; Yao, Y. B.; Tao, T.; Liang, B.; Lin, X. W.; Guo, J. H.; Zeng, Y. J.; Lu, S. G. Enhanced electrocaloric effect in Sr^{2+} -modified lead-free $BaZr_xTi_{1-x}O_3$ ceramics. ACS Appl. Mater. Interfaces 2019, 11 (22), 20167–20173.
- (42) Jin, L.; Huo, R.; Guo, R.; Li, F.; Wang, D.; Tian, Y.; Hu, Q.; Wei, X.; He, Z.; Yan, Y.; et al. Diffuse phase transitions and giant electrostrictive coefficients in lead-free Fe³⁺-doped 0.5Ba(Zr_{0.2}Ti_{0.8}O₃-0.5)Ba_{0.7}Ca_{0.3}TiO₃ ferroelectric ceramics. *ACS Appl. Mater. Interfaces* **2016**, 8 (45), 31109–31119.
- (43) Yang, T.; Ke, X.; Wang, Y. Mechanisms responsible for the large piezoelectricity at the tetragonal-orthorhombic phase boundary of (1-x)BaZr_{0.2}Ti_{0.8}O₃-xBa_{0.7}Ca_{0.3}TiO₃ system. *Sci. Rep.* **2016**, *6*, 33392.
- (44) Keswani, B. C.; Devan, R. S.; Kambale, R. C.; James, A. R.; Manandhar, S.; Kolekar, Y. D.; Ramana, C. V. Correlation between structural, magnetic and ferroelectric properties of Fe-doped (Ba-Ca)TiO₃ lead-free piezoelectric. *J. Alloys Compd.* **2017**, *712*, 320–333.
- (45) Jian, G.; Jiao, Y.; Meng, Q.; Shao, H.; Wang, F.; Wei, Z. 3D ${\rm BaTiO_3}$ flower based polymer composites exhibiting excellent piezoelectric energy harvesting properties. *Adv. Mater. Interfaces* **2020**, 7 (16), 2070089.
- (46) Bersuker, I. B.; Polinger, V. Perovskite crystals: Unique pseudojahn-teller origin of ferroelectricity, multiferroicity, permittivity, flexoelectricity, and polar nanoregions. *Condens. Matter* **2020**, *5*, 68.
- (47) Li, J.; Wei, X.; Sun, X. X.; Li, R.; Wu, C.; Liao, J.; Zheng, T.; Wu, J. A novel strategy for excellent piezocatalytic activity in lead-free BaTiO₃-based materials via manipulating the multiphase coexistence. *ACS Appl. Mater. Interfaces* **2022**, *14* (41), 46765–46774.
- (48) Lin, Q.; Wang, D.; Chen, Z.; Liu, W.; Lim, S.; Li, S. Periodicity dependence of the built-in electric field in $(Ba_{0.7}Ca_{0.3})TiO_3/Ba(Zr_{0.2}Ti_{0.8})O_3$ ferroelectric superlattices. ACS Appl. Mater. Interfaces **2015**, 7 (47), 26301–26306.
- (49) Liu, Y.; Chang, Y.; Li, F.; Yang, B.; Sun, Y.; Wu, J.; Zhang, S.; Wang, R.; Cao, W. Exceptionally high piezoelectric coefficient and low strain hysteresis in grain-oriented (Ba, Ca)(Ti,Zr)O₃ through integrating crystallographic texture and domain engineering. ACS Appl. Mater. Interfaces 2017, 9 (35), 29863–29871.
- (50) Mahajan, S.; Thakur, O. P.; Prakash, C.; Sreenivas, K. Effect of Zr on dielectric, ferroelectric and impedance properties of $BaTiO_3$ ceramic. *Bull. Mater. Sci.* **2011**, *34* (7), 1483–1489.
- (51) Liu, Y.; Chang, Y.; Sun, E.; Li, F.; Zhang, S.; Yang, B.; Sun, Y.; Wu, J.; Cao, W. Significantly enhanced energy-harvesting performance and superior fatigue-resistant behaviour in [001]_c-textured BaTiO₃-

- based lead-free piezoceramics. ACS Appl. Mater. Interfaces 2018, 10 (37), 31488-31497.
- (52) Lu, H.; Zhang, J.; Yang, L.; Zhang, Y.; Wu, Y.; Zheng, H. Enhanced output performance of piezoelectric nanogenerators by Tb-modified (BaCa)(ZrTi)O₃ and 3D core/shell structure design with PVDF composite spinning for microenergy harvesting. ACS Appl. Mater. Interfaces 2022, 14 (10), 12243–12256.
- (53) Lv, X.; Zhang, J.; Liu, Y.; Li, F.; Zhang, X. X.; Wu, J. Synergetic contributions in phase boundary engineering to the piezoelectricity of potassium sodium niobate lead-free piezoceramics. *ACS Appl. Mater. Interfaces* **2020**, *12* (35), 39455–39461.
- (54) Zhu, X. N.; Zhang, W.; Chen, X. M. Enhanced dielectric and ferroelectric characteristics in Ca-modified BaTiO₃ ceramics. *AIP Adv.* **2013**, *3* (8), 082125.
- (55) Wang, X.; Yamada, H.; Xu, C. N. Large electrostriction near the solubility limit in BaTiO₃-CaTiO₃ ceramics. *Appl. Phys. Lett.* **2005**, *86* (2), 022905.
- (56) Adachi, M. A. Y.; Asahi, T.; Deguchi, K.; Gesi, K.; Hasebe, K.; Hikita, T.; Ikeda, T.; Iwata, Y. Ferroelectrics and Related Substances: Oxides Part 1: Perovskite-type oxides and LiNbO₃ family; Landolt-Börnstein, New Series III/36A1, 2001; Vol. 36, pp 1–1727.
- (57) Robins, L. H.; Kaiser, D. L.; Rotter, L. D.; Schenck, P. K.; Stauf, G. T.; Rytz, D. Investigation of the structure of barium titanate thin films by Raman spectroscopy. *J. Appl. Phys.* **1994**, *76* (11), 7487–7498.
- (58) Fernandez-Benavides, D. A.; Gutierrez-Perez, A. I.; Benitez-Castro, A. M.; Ayala-Ayala, M. T.; Moreno-Murguia, B.; Munoz-Saldana, J. Comparative study of ferroelectric and piezoelectric properties of BNT-BKT-BT ceramics near the phase transition zone. *Materials* **2018**, *11* (3), 361.
- (59) Gutierrez, G.; Sundin, E. M.; Nalam, P. G.; Zade, V.; Romero, R.; Nair, A. N.; Sreenivasan, S.; Das, D.; Li, C.; Ramana, C. V. Interfacial phase modulation-induced structural distortion, band gap reduction, and nonlinear optical activity in Tin-incorporated Ga₂O₃. *J. Phys. Chem. C* **2021**, *125*, 20468–20481.
- (60) Bharathi, K. K.; Tackett, R. J.; Botez, C. E.; Ramana, C. V. Coexistence of spin glass behavior and long-range ferrimagnetic ordering in La-and Dy-doped Co ferrite. *J. Appl. Phys.* **2011**, *109*, 07A510.
- (61) Sun, Y.; Liu, D.; Li, Q.; Shim, J.; He, W.; Fang, H.; Yan, Q. Piezoelectric property of a tetragonal (Ba,Ca)(Zr,Ti)O₃ single crystal and its fine-domain structure. *ACS Appl. Mater. Interfaces* **2018**, *10* (15), 12847–12853.
- (62) Wang, C.; Gao, X.; Zheng, M.; Zhu, M.; Hou, Y. Two-step regulation strategy improving stress transfer and poling efficiency boosts piezoelectric performance of 0–3 piezocomposites. *ACS Appl. Mater. Interfaces* **2021**, *13* (35), 41735–41743.
- (63) Keswani, B. C.; Patil, S. I.; James, A. R.; Kolekar, Y. D.; Ramana, C. V. Correlation between structural, ferroelectric, piezoelectric and dielectric properties of Ba_{0.7}Ca_{0.3}TiO₃-xBaTi_{0.8}Zr_{0.2}O₃ (x = 0.45, 0.55) ceramics. *Ceram. Int.* **2018**, 44, 20921–20928.
- (64) Kalidindi, N. R.; Manciu, F. S.; Ramana, C. V. Crystal structure, phase, and electrical conductivity of nanocrystalline $W_{0.95}Ti_{0.05}O_3$ thin films. ACS Appl. Mater. Interfaces 2011, 3, 863–868.
- (65) Hussain, O. M.; Srinivasa Rao, K.; Madhuri, K. V.; Ramana, C. V.; Naidu, B. S.; Pai, S.; John, J.; Pinto, R. Growth and characteristics of reactive pulsed laser deposited molybdenum trioxide thin films. *Appl. Phys. A: Mater. Sci. Process.* **2002**, *75*, 417–422.
- (66) Mu, X.; Chen, X.; Wang, J.; Sun, M. Visualizations of electric and magnetic interactions in electronic circular dichroism and Raman optical activity. *J. Phys. Chem. A* **2019**, *123*, 8071–8081.
- (67) Nafie, L. A. Vibrational Optical Activity: From Small Chiral Molecules to Protein Pharmaceuticals and Beyond. *Front. Adv. Mol. Spectrosc.* **2018**, 421–469.
- (68) Troitskaia, I. B.; Gavrilova, T. S. A.; Gromilov, S. A.; Sheglov, D. V.; Atuchin, V. V.; Vemuri, R. S.; Ramana, C. V. Growth and structural properties of α -MoO₃(010) microplates with atomically flat surface. *Mater. Sci. Eng., B* **2010**, 174, 159–163.

- (69) Ramana, C. V.; Ait-Salah, A.; Utsunomiya, S.; Morhange, J. F.; Mauger, A.; Gendron, F.; Julien, C. M. Spectroscopic and chemical imaging analysis of Lithium Iron triphosphate. *J. Phys. Chem. C* **2007**, *111* (2), 1049–1054.
- (70) Ramana, C. V.; Ait-Salah, A.; Utsunomiya, S.; Mauger, A.; Gendron, F.; Julien, C. M. Novel Lithium Iron Pyrophosphate (LiFe1.5P2O7) as a Positive Electrode for Li-Ion Batteries. *Chem. Mater.* **2007**, *19* (22), 5319–5324.
- (71) Bouaamlat, H.; Hadi, N.; Belghiti, N.; Sadki, H.; Naciri Bennani, M.; Abdi, F.; Lamcharfi, T.; Bouachrine, M.; Abarkan, M. Dielectric properties, AC conductivity, and electric modulus analysis of bulk ethylcarbazole-terphenyl. *Adv. Mater. Sci. Eng.* **2020**, 2020, 1—8.
- (72) Keswani, B. C.; Patil, S. I.; James, A. R.; Nath, R. C.; Boomishankar, R.; Kolekar, Y. D.; Ramana, C. V. Structural, magnetic and ferroelectric properties of lead free piezoelectric 0.9-(0.45Ba_{0.7}Ca_{0.3}TiO₃-0.55BaTi_{0.8}Zr_{0.2}O₃) and magnetostrictive 0.1-(Co_{0.7}Mn_{0.3}Fe_{1.95}Dy_{0.05}O₄) magnetoelectric particulate composite. *J. Appl. Phys.* **2019**, *126*, 224101.
- (73) Dorey, R. A. Ceramic thick films for MEMS and microdevices ebook; William Andrew, Elsevier, 2011; pp 1–191.
- (74) Wang, W.; Chen, Z.; Zhou, Z.; Li, Y.; Liang, R. Enhancing electromechanical properties of PZT-based piezoelectric ceramics by high-temperature poling for high-power applications. *ACS Appl. Mater. Interfaces* **2023**, *15* (12), 15636–15645.
- (75) Wang, Y.; Wang, D.; Xu, J.; Zhong, L.; Gao, J.; Xiao, A.; Wu, M.; He, Z.; Yao, R.; Li, S.; et al. Trirelaxor ferroelectric material with giant dielectric permittivity over a wide temperature range. *ACS Appl. Mater. Interfaces* **2021**, *13* (28), 33272–33281.
- (76) Kuang, S. J.; Tang, X. G.; Li, L. Y.; Jiang, Y. P.; Liu, Q. X. Influence of Zr dopant on the dielectric properties and Curie temperatures of $Ba(Zr_xTi_{1-x})O_3$ ($0 \le x \le 0.12$) ceramics. *Scr. Mater.* **2009**, *61* (1), 68–71.
- (77) Tu, C. S.; Jou, Y. S.; Chen, P. Y.; Chen, C. S.; Hsu, Y. C.; Feng, K. C.; Chien, R. R.; Schmidt, V. H.; Haw, S. C. Enhancing photovoltaic and photosensing performances in bismuth ferrite via polar order engineering. *ACS Appl. Electron. Mater.* **2020**, 2 (11), 3773–3782.
- (78) Vats, G.; Peräntie, J.; Palosaari, J.; Juuti, J.; Seidel, J.; Bai, Y. Current modulation by optoelectric control of ferroelectric domains. *ACS Appl. Electron. Mater.* **2020**, 2 (9), 2829–2836.
- (79) Zhang, M.; Zhang, H.; Jiang, Q.; Gao, F.; Chen, R.; Zhang, D.; Reece, M. J.; Yang, B.; Viola, G.; Yan, H. Terahertz characterization of lead-free dielectrics for different applications. *ACS Appl. Mater. Interfaces* **2021**, *13* (45), 53492–53503.
- (80) Salaeh, S.; Das, A.; Stöckelhuber, K. W.; Wießner, S. Fabrication of a strain sensor from a thermoplastic vulcanizate with an embedded interconnected conducting filler network. *Composites, Part A* **2020**, 105763.
- (81) Viola, G.; Saunders, T.; Wei, X.; Chong, K. B.; Luo, H.; Reece, M. J.; Yan, H. Contribution of piezoelectric effect, electrostriction and ferroelectric/ferroelastic switching to strain-electric field response of dielectrics. *J. Adv. Dielectr.* **2013**, *03*, 1350007.
- (82) Mezheritsky, A. V. Quality factor of piezoceramics. *Ferroelectrics* **2002**, *266*, 277–304.
- (83) Pertsev, N. A.; Dkhil, B. Strain sensitivity of polarization in perovskite ferroelectrics. *Appl. Phys. Lett.* **2008**, *93*, 122903.
- (84) Keeble, D. S.; Benabdallah, F.; Thomas, P. A.; Maglione, M.; Kreisel, J. Revised structural phase diagram of (Ba_{0.7}Ca_{0.3}TiO₃)-(BaZr_{0.2}Ti_{0.8}O₃). *Appl. Phys. Lett.* **2013**, *102*, 092903.
- (85) Wu, J. Perovskite lead-free piezoelectric ceramics. *J. Appl. Phys.* **2020**, *127*, 190901 1–13.
- (86) Lupascu, D. C. Fatigue in Ferroelectric Ceramics and Related Issues; Springer Science & Business Media, 2004; pp 1–228.
- (87) Praveen, J. P.; Kumar, K.; James, A. R.; Karthik, T.; Asthana, S.; Das, D. Large piezoelectric strain observed in sol-gel derived BZT-BCT ceramics. *Curr. Appl. Phys.* **2014**, *14*, 396–402.
- (88) Baraskar, B. G.; Kadhane, P. S.; Darvade, T. C.; James, A. R.; Kambale, R. C. BaTiO₃-based lead-free electroceramics with their

- ferroelectric and piezoelectric properties tuned by Ca²⁺, Sn⁴⁺ and Zr⁴⁺ substitution useful for electrostrictive device application. In *In Ferroelectrics and Their Applications*; IntechOpen, 2018; pp 114–132.
- (89) Uchino, K. Electrostrictive and piezoelectric effects in relaxor ferroelectrics: Historical background. *IEEE Trans. Ultrason. Eng.* **2022**, 69 (11), 3013–3036.
- (90) Chen, H.; Shen, B.; Xu, J.; Zhai, J. The grain size-dependent electrical properties of $Bi_4Ti_3O_{12}$ piezoelectric ceramics. *J. Alloys Compd.* **2013**, 551, 92–97.
- (91) Zhang, L.; Zhao, L.; He, L.; Wang, D.; Sun, Y.; Wang, D.; Lou, X.; Zhang, L.; Carpenter, M. A. New degree of freedom in determining superior piezoelectricity at the lead-free morphotropic phase boundary: The invisible ferroelectric crossover. *ACS Appl. Mater. Interfaces* **2022**, *14* (1), 1434–1442.
- (92) Nor, N. M.; Hamzah, H. H.; Abdul Razak, K. Chapter 9 Recent advancement in sustainable energy harvesting using piezo-electric materials. In *In Sustainable Materials for Next Generation Energy Devices*; Cheong, K. Y., Chen, L. C., Eds.; Elsevier, 2021; pp 221–248.
- (93) Zhao, K.; Zheng, M.; Yan, X.; Zhu, M.; Hou, Y. Tailored ceramic—metal piezocomposite energy harvester with high current output by controlling the electrical impedance. *ACS Appl. Electron. Mater.* **2022**, *4* (7), 3679–3685.
- (94) Takenaka, T. Chapter 4 Lead-free piezo-ceramics. In *Advanced Piezoelectric Materials, Science and Technology*; Woodhead Publishing Series in Electronic and Optical Materials, 2010; pp 130–170.
- (95) Potong, R.; Rianyoi, R.; Ngamjarurojana, A.; Chaipanich, A. Dielectric and piezoelectric properties of 1–3 non-lead barium zirconate titanate-portland cement composites. *Ceram. Int.* **2013**, *39*, S53–S57.
- (96) Sharma, P.; Kumar, P.; Kundu, R. S.; Ahlawat, N.; Punia, R. Enhancement in magnetic, piezoelectric and ferroelectric properties on substitution of titanium by iron in barium calcium titanate ceramics. *Ceram. Int.* **2016**, *42* (10), 12167–12171.
- (97) Brajesh, K.; Tanwar, K.; Abebe, M.; Ranjan, R. Relaxor ferroelectricity and electric-field-driven structural transformation in the giant lead-free piezoelectric (Ba,Ca)(Ti,Zr)O₃. *Phys. Rev. B* **2015**, 92 (22), 224112.
- (98) Roy, S.; Maharana, R.; Reddy, S. R.; Singh, S.; Kumar, P.; Karthik, T.; Asthana, S.; Prasad, V. V. B.; Kamat, S. V. Structural, ferroelectric and piezoelectric properties of chemically processed, low temperature sintered piezoelectric BZT-BCT ceramics. *Mater. Res. Express* **2016**, 3 (3), 035702.